Sensitivity of Ozone Dry Deposition to Ecosystem-Atmosphere Interactions: A Critical Appraisal of Observations and Simulations

Meiyun Lin[1,2] (ID), Sergey Malyshev[2] (ID), Elena Shevliakova[2] (ID), Fabien Paulot[1,2] (ID), Larry W. Horowitz[2] (ID), Silvano Fares[3] (ID), Teis N. Mikkelsen[4] (ID), and Leiming Zhang[5] (ID)

[1]Program in Atmospheric and Oceanic Sciences, Princeton University, Princeton, NJ, USA, [2]NOAA Geophysical Fluid Dynamics Laboratory, Princeton, NJ, USA, [3]Council for Agricultural Research and Economics, Research Centre for Forestry and Wood, Rome, Italy, [4]Department of Environmental Engineering, Technical University of Denmark, Lyngby, Denmark, [5]Air Quality Research Division, Science and Technology Branch, Environment and Climate Change Canada, Toronto, Ontario, Canada

Abstract The response of ozone (O_3) dry deposition to ecosystem-atmosphere interactions is poorly understood but is central to determining the potential for extreme pollution events under current and future climate conditions. Using observations and an interactive dry deposition scheme within two dynamic vegetation land models (Geophysical Fluid Dynamics Laboratory LM3.0/LM4.0) driven by observation-based meteorological forcings over 1948–2014, we investigate the factors controlling seasonal and interannual variability (IAV) in O_3 deposition velocities ($V_{d,O3}$). Stomatal activity in this scheme is determined mechanistically, depending on phenology, soil moisture, vapor pressure deficit, and CO_2 concentration. Soil moisture plays a key role in modulating the observed and simulated $V_{d,O3}$ seasonal changes over evergreen forests in Mediterranean Europe, South Asia, and the Amazon. Analysis of multiyear observations at forest sites in Europe and North America reveals drought stress to reduce $V_{d,O3}$ by ~50%. Both LM3.0 and LM4.0 capture the observed $V_{d,O3}$ decreases due to drought; however, IAV is weaker by a factor of 2 in LM3.0 coupled to atmospheric models, particularly in regions with large precipitation biases. IAV in summertime $V_{d,O3}$ to forests, driven primarily by the stomatal pathway, is largest (15–35%) in semiarid regions of western Europe, eastern North America, and northeastern China. Monthly mean $V_{d,O3}$ for the highest year is 2 to 4 times that of the lowest, with significant implications for surface O_3 variability and extreme events. Using $V_{d,O3}$ from LM4.0 in an atmospheric chemistry model improves the simulation of surface O_3 abundance and spatial variability (reduces mean biases by ~10 ppb) relative to the widely used Wesely scheme.

1. Introduction

Tropospheric ozone (O_3) is a potent greenhouse gas and biological oxidant detrimental to human health and vegetation and is central to the atmospheric chemistry controlling the removal of numerous hazardous trace gases. Dry deposition to the Earth's surface accounts for 20% of the annual global tropospheric O_3 loss according to atmospheric chemistry model estimates (Stevenson et al., 2006; Young et al., 2013). Dry deposition varies substantially across land types and ecosystems (Wesely, 1989) and represents an important control on near-surface O_3 concentrations (Wild, 2007). Over many parts of the world, land-atmosphere interactions can modulate the dynamics of regional climate and ecosystem functioning (e.g., Seneviratne et al., 2006). The response of O_3 dry deposition to ecosystem-atmosphere interactions is poorly understood, owing to a lack of reliable long-term observations and process-based model formulations (Fowler et al., 2009; Wu et al., 2018), but may influence extreme pollution events and susceptibility to climate change (Andersson & Engardt, 2010; Emberson et al., 2013; Gerosa et al., 2009; Lin et al., 2017). Here we systematically investigate the factors controlling the seasonal and interannual variability in O_3 deposition velocities ($V_{d,O3}$), using a suite of observations and dynamic vegetation land model hindcast simulations (1948–2014) including a new interactive dry deposition scheme.

The rate of dry deposition of ozone to vegetated surfaces during daytime is typically limited by the canopy resistance (Mikkelsen et al., 2004; Pilegaard et al., 1995; Wu et al., 2018), which has stomatal and nonstomatal pathways (Ganzeveld et al., 2015). Stomata, small pores in the leaf, are responsible for controlling CO_2

AGU
100
ADVANCING EARTH
AND SPACE SCIENCE

Global Biogeochemical Cycles

10.1029/2018GB006157

transport for photosynthesis and water vapor losses; they also permit the uptake of O_3 and other pollutants by vegetation. The stomatal uptake of O_3 is largely regulated by the physiological activity and associated gas exchanges of the vegetation, with light, temperature, and water availability in the plant-soil system as the dominant controlling factors (Fowler et al., 2009). Under drought stress, plants close their stomata to conserve water, consequently limiting the O_3 uptake by vegetation, affecting the observed seasonal cycle and interannual variability in daytime $V_{d,O3}$ (Fares et al., 2014; Gerosa et al., 2009; Gerosa, Finco, Mereu, Vitale, et al., 2009; Matsuda et al., 2006; Rummel et al., 2007). There is also observational evidence that rising atmospheric CO_2 concentrations cause stomatal conductance to decrease (Lammertsma et al., 2011; Long et al., 2004). Field work suggests that nonstomatal O_3 sinks (including chemical reactions in the canopy air and deposition to plant and soil surfaces) are not constant but vary with environmental variables, such as surface temperature, humidity, canopy wetness, friction velocity, and biogenic volatile organic compounds or nitrogen oxides (NO_x) in canopy air (Clifton, 2018; Coyle et al., 2009; El-Madany et al., 2017; Fares et al., 2010; Stella et al., 2011; Zhang et al., 2002). More recently, Clifton et al. (2019) reported that suppression of soil uptake when soil is wet may explain observed interannual variability in $V_{d,O3}$ over a deciduous forest.

Current large-scale chemical transport models (CTMs; Kukkonen et al., 2012; Hardacre et al., 2015; Morgenstern et al., 2017) typically include a variant of the Wesely (1989) parameterization ("the Wesely scheme") to calculate dry deposition. With a resistance-in-series framework, the Wesely scheme is well suited for inclusions in global models and has success in some applications when evaluating observed and modeled monthly mean climatology of $V_{d,O3}$ averaged globally across sites for a particular land cover type (Silva & Heald, 2018; Val Martin et al., 2014; Wesely & Hicks, 2000). However, the substantial interannual variability and site-to-site differences in $V_{d,O3}$ derived from measurements are not simulated by CTMs with the Wesely scheme driven by observed meteorology (Clifton et al., 2017; Silva & Heald, 2018). The expression for stomatal resistance used in the Wesely scheme is dependent on only solar radiation, air temperature, and leaf area index (LAI; Wesely, 1989; Kavassalis & Murphy, 2017). The lack of sensitivity to water availability is problematic: For example, the Wesely scheme fails to simulate the observed $V_{d,O3}$ decreases over a Mediterranean forest during the August 2003 European drought (Rydsaa et al., 2016). CTMs not accounting for the effect of water availability on O_3 stomatal deposition typically underestimate the highest observed surface O_3 levels during severe drought events (Lin et al., 2017).

The nonstomatal deposition schemes as implemented in many models do not vary with meteorology, aside from some parameters prescribed for each season and each land cover, thereby missing many processes that can affect this deposition pathway, as suggested by field measurements (Clifton et al., 2019; Fares et al., 2010; Fowler et al., 2009; Rannik et al., 2012). Based on analysis of O_3 flux measurements at five sites in North America, Zhang et al. (2003) developed a new scheme that parameterized nonstomatal resistance as a function of friction velocity, relative humidity, LAI, and canopy wetness ("the Zhang scheme"). Although these developments were applied in some regional models (Kukkonen et al., 2012), they have not generally been implemented in global-scale CTMs. Furthermore, these models typically do not include the influence of in-canopy chemistry, through which O_3 may be scavenged by reactive biogenic volatile organic compounds or NO_x (Fares et al., 2010).

A few more recent regional CTMs (Emberson et al., 2013; Huang et al., 2016; Simpson et al., 2012) do parameterize the effect of soil moisture on stomatal conductance, following Jarvis (1976) in assuming that environmental factors act independently in determining stomatal conductance. In reality, the stomatal response to individual variables is complex and usually nonlinear (Leuning, 1995). Some global land-carbon cycle models include the effects of O_3 exposure on photosynthesis and stomatal conductance (Lombardozzi et al., 2015; Sitch et al., 2007). Val Martin et al. (2014) showed that coupling to vegetation phenology improved the simulation of $V_{d,O3}$ seasonality in a chemistry-climate model. The O_3 stomatal deposition in their model was based on the Ball-Berry conductance scheme, which does not account for stomatal closure under soil drying. Importantly, process-oriented evaluation of observed and simulated $V_{d,O3}$ interannual variability at sites around the globe is lacking in the published literature.

Advancing knowledge concerning sources of $V_{d,O3}$ variability on daily to multidecadal time scales, particularly responses to ecosystem-atmosphere interactions and the feedbacks on surface air quality, requires that process-based, rather than empirical, dry deposition parameterizations be implemented in chemistry-climate

models. In this work, we apply the new interactive dry deposition scheme of Paulot et al. (2018) to represent O_3 deposition in National Oceanic and Atmospheric Administration's Geophysical Fluid Dynamics Laboratory (GFDL) dynamic vegetation land models (LM3.0/LM4.0; Shevliakova et al., 2009; Milly et al., 2014; Zhao et al., 2018b; a), driven by observed atmospheric forcings (Sheffield et al., 2006) or coupled to National Oceanic and Atmospheric Administration's GFDL atmospheric chemistry-climate models (AM3/ AM4; Donner et al., 2011; Zhao et al., 2018b). Incorporated into a combined stomatal-photosynthesis model, this scheme mechanistically describes the response of stomatal conductance to phenology, CO_2 concentration, temperature, canopy air vapor pressure deficit, and soil water availability. We analyze a suite of observations alongside the model simulations for the past half century to assess the underlying processes controlling O_3 deposition across the globe. Specifically, our analyses focus on examining the influence of regional and local environmental variables (e.g., drought stress) on $V_{d,O3}$ variability on seasonal to interannual time scales.

Section 2 briefly describes $V_{d,O3}$ observations, model formulations, and experiments. We begin our analysis by investigating factors controlling the seasonal cycle of $V_{d,O3}$, including the spatial distributions of vegetation types, critical leaf temperature, and water availability (section 3). We then use observations and model simulations to examine interannual variability of $V_{d,O3}$ during the growing season and the relationship of $V_{d,O3}$ to drought and precipitation (section 4). Section 5 summarizes the global-to-regional distributions of O_3 deposition to the major land cover classes, quantifies the contributions of stomatal versus nonstomatal pathways, identifies the regions in the world with the largest interannual variability in $V_{d,O3}$, and draws implications concerning the deployment of future measurements. In section 6, we examine the influence on surface O_3 simulations from the shift of $V_{d,O3}$ from the Wesely scheme to the new scheme as implemented in GFDL LM4.0. Specifically, we leverage the Tropospheric Ozone Assessment Report (TOAR) Surface Ozone Database with vast spatial coverage around the world (Schultz et al., 2017) and a new data set over China (https://www.aqistudy.cn) to assess the two deposition schemes. Finally, we synthesize in section 7 the model strengths and limitations, discuss the implications, and make recommendations for future O_3 flux measurements.

2. Methods

2.1. Ozone Dry Deposition Observations

We compile a suite of field-based $V_{d,O3}$ observations at 41 locations, obtained from 26 literature sources published between 1990 and 2018 (Table 1). Model evaluations are conducted on a site-by-site basis for the purpose of examining the influence from regional to local meteorology and land cover. Sites with continuous measurements for at least 2 years are used to evaluate the seasonal cycle of $V_{d,O3}$ (section 3). To explore the influence of water availability on $V_{d,O3}$ seasonality, observations are separated into the dry and wet seasons for evergreen forest sites in Mediterranean Europe (Castelporziano, Italy), South Asia (Mea Moh and Datum Valley), and the Amazon. Multiyear measurements at a boreal forest in Denmark (1996–2000) and a deciduous forest in Ontario, Canada (2008–2013), are analyzed for the influence of drought stress on $V_{d,O3}$ interannual variability (section 4). For short-term observations, we focus on daytime average (9 a.m. to 3 p.m.) for the growing season (June-July-August, JJA) to evaluate the modeled spatial variability of $V_{d,O3}$ across North America and Europe (section 5). For comparison with observations, we sample modeled $V_{d,O3}$ to the land cover tile that best matches the observed vegetation type at individual sites (as opposed to using a grid cell average). Given the heterogeneity of land surface properties and the uncertainty in both the land model forcing data set and O_3 flux measurements themselves at finer temporal scales (i.e., daily to weekly), we focus on evaluating the most salient processes influencing seasonal to interannual variability in $V_{d,O3}$.

2.2. Model Formulations and Experiments

Paulot et al. (2018) developed an interactive dry deposition scheme in GFDL LM3.0 and evaluated the dry deposition velocities and fluxes of reactive nitrogen species. Here we evaluate and improve the dry deposition scheme for O_3 in LM3.0 and an updated version of the land model, LM4.0. LM4.0 is a new model of terrestrial water, energy, and carbon, intended for use in global hydrological analyses and as a component of GFDL Earth system and physical climate models contributing to the Coupled Model Intercomparison Project, Phase 6 (Zhao et al., 2018a, 2018b). Both LM3.0 and LM4.0 include five vegetation types (C3 and C4 grasses, and temperate deciduous, tropical, and cold evergreen trees) and describe small-scale heterogeneity of

Table 1
Characteristics of the $V_{d,O3}$ Measurement Sites

Sites	Latitude	Longitude	Observed land cover	Model land class	LAI	Sampling height	Sampling period	Method	Daytime $V_{d,O3}$ (cm/s)	References
Evergreen tropical forests										
Mea Moh, Thailand	18.28°N	99.72°E	Tropical forest	Natural	?	15 m, 23 m	Jan–April 2002	Gradient	0.32 (dry)	Matsuda et al. (2005)
Mea Moh, Thailand	18.28°N	99.72°E	Tropical forest	Natural	?	15 m, 23 m	Jan–Apr 2004 May–Aug 2004	Gradient	0.38 (dry) 0.64 (wet)	Matsuda et al. (2006)
Datum Valley, Borneo	4.98°N	117.85°E	Rainforest	Natural	6	45 m	July 2008	Eddy covariance	0.9 (wet)	Fowler et al. (2011)
Central Amazon, Brazil	3.0°S	59.9°W	Rainforest	Natural	7	39 m	22 Apr to 8 May 1987	Eddy covariance	1.8 (wet)	Fan et al. (1990)
Southwest Amazon, Brazil	10.1°S	61.9°W	Rainforest	Natural	5.6	53 m	4–22 May 1999 Sep–Oct 1999	Eddy covariance	1.1 (wet) 0.5 (dry)	Rummel et al. (2007)
European forests										
Hyytiala, Finland	61.85°N	24.28°E	Scots pine forest	Natural	6.0–8.0	23 m	2001–2010	Eddy covariance	0.54	Rannik et al. (2012)
Ulborg, Denmark	56.28°N	8.42°E	Coniferous	Natural	8	18 m, 36 m	1996–2000	Gradient	0.92	Mikkelsen et al. (2004)
Auchencorth Moss, Scotland	55.78°N	3.23°W	Moorland	Secondary	2	0.3–3.0 m	1995–1998	Gradient	0.65	Fowler et al. (2001)
Bily Kriz, Czech Republic	49.55°N	18.53°E	Coniferous	Secondary	9–9.5	36 m	July–August 2008	Gradient	0.50	Zapletal et al. (2011)
Alice Holt, UK	51.17°N	0.84°W	Deciduous	Natural	?	13 m	16 July to 18 August 2005	Eddy covariance	0.85	Fowler et al. (2009)
Les Landes Forest, France	44.20°N	0.70°W	Pine, deciduous	Natural	2.1	36 m	June 1994	Eddy	0.62	Lamaud et al. (2002)
Castelporziano, Italy	41.70°N	12.35°E	Holm Oak	Natural	3.7	19.7 m	2012–2013	Eddy covariance	0.40 (wet) 0.29 (dry)	Fares et al. (2014)
North American forests										
Blodgett Forest, California	38.90°N	120.63°W	Pine plantation	Natural	3.6	12 m	June 1999 to June 2000	Eddy covariance	0.50	Kurpius et al. (2002)
Blodgett Forest, California	38.88°N	120.62°W	Pine plantation	Natural	1.2–2.9	12.5 m	2001–2007	Eddy covariance	0.92	Fares et al. (2010)
Citrus Orchard	36.35°N	119.09°W	Citrus Orchard	Secondary	3.0	1.0–9.2 m	Oct 2009 to Nov 2010	Eddy covariance	0.37	Fares et al. (2012)
Manitou Forest, Colorado	39.10°N	105.10°W	Pine plantation	Natural	?	12 m, 25 m	7–31 August 2010	Gradient	0.50	Park et al. (2014)
Niwot Ridge, Colorado	40.03°N	105.55°W	Pine plantation	Natural	4.2	27 m	May–August 2002–2005	Eddy covariance	0.39	Turnipseed et al. (2009)
Ontario, Canada	44.32°N	80.93°W	Deciduous	Natural	5.0	33.4 m	Summer 1988	Eddy covariance	1.00	Padro (1996)
Ontario, Canada	44.19°N	79.56°W	Deciduous	Natural	4.6	16 m,33 m	2008–2013	Gradient	0.91	Wu et al. (2016)
Sand Flats, New York	43.57°N	75.24°W	Deciduous	Natural	5.0–6.0	36 m	May–October 1998	Eddy covariance	0.82	Finkelstein et al. (2000)
Harvard Forest, MA	42.53°N	72.18°W	Deciduous	Natural	3.4	30 m	1990–2000	Eddy covariance	0.70	Munger et al. (1996)
Kane, Pennsylvania	41.60°N	78.77°W	Deciduous	Natural	5.0–7.0	36 m	April–October 1997	Eddy covariance	0.83	Finkelstein et al. (2000)
Duke Forest, North Carolina	35.97°N	79.13°W	Deciduous	Natural	?	21 m	April–May 1996	Eddy covariance	0.80	Finkelstein et al. (2000)
Croplands										
Gilchriston, Scotland	55.90°N	2.80°W	Potatoes	Cropland	?	?	July–August 2006	Eddy covariance	0.76	Coyle et al. (2009)
Grignon, France	48.85°N	1.97°E	Maize crop	Cropland	5.2	3.4 m	June–August 2008	Eddy covariance	0.63	Stella et al. (2011)

La CapeSud, France	44.30°N	0.63°W	Maize crop	5.1	6.4 m	June–August 2008	Eddy covariance	0.50	Stella et al. (2011)
Lamasquere, France	43.82°N	1.38°E	Maize crop	3.2	3.65 m	June–August 2008	Eddy covariance	0.38	Stella et al. (2011)
Bondville, Illinois	40.05°N	88.37°W	Corn	2.4–3	?	18 August to 1 October 1994	Eddy covariance	0.6	Meyers et al. (1998)
Nashville, Tennesse	36.65°N	87.03°W	Soybeans	1.0–6.0	4.55 m	22 June to 11 October 1995	Eddy covariance	0.7	Meyers et al. (1998)
Grassland/Pasture			Pasture						
Mean of 11 data sets								0.4	Silva and Heald (2018) and references therein

Note. The 9 a.m to 3 p.m. average values in centimeters per second are reported for the daytime values for the growing season (June-July-August) are reported. The ? mark indicates that the information was not reported in the literature. LAI = leaf area index. For the other vegetation types, only the dry and wet seasons, respectively, for evergreen tropical forests.

land surface cover in each grid cell using a mosaic approach, as a combination of subgrid tiles in four land use categories: lands undisturbed by human activity (i.e., "primary" or "natural"), cropland, pasture, and lands harvested at least once (i.e., "secondary"), including managed forests and abandoned croplands and pastures (Malyshev et al., 2015; Shevliakova et al., 2009). Planting and harvesting dates for crops as well as pasture grazing are updated as described by Paulot et al. (2018). Neither of the land model configurations used in this study includes treatment of irrigation or of nitrogen limitation on plant growth.

LM3.0 uses a 2° latitude × 2.5° longitude grid and is configured similarly to the land component of GFDL ESM 2Mb (Dunne et al., 2012; Malyshev et al., 2015), except for the updates on cropping dates and pasture grazing. LM4.0 employs a cubed-sphere grid resolution of ~100 × 100 km^2 and serves as the land component for the new set of GFDL AM4/CM4 models (Zhao et al., 2018a, 2018b). Motivated by biases in LM3.0 simulations, the standard version of LM4.0 includes the following updates: (1) decreasing the cold season length threshold to better locate the cold evergreen-temperate deciduous forest boundary; (2) decreasing critical leaf temperature to better match the seasonal green-up as inferred from Moderate Resolution Imaging Spectroradiometer (MODIS) reflectances; (3) using a more physically based approach for drought-induced leaf drop; (4) changing soil types and parameters affecting surface albedo, plant hydraulics, and biogeography (see Section 10 in Zhao et al., 2018a); and (5) limiting the maximum LAI attainable by the vegetation on the basis of light availability. The aforementioned Updates (1) to (3) follow parameterizations previously implemented in LM3.1, as described by Milly et al. (2014). In the LM4.0 experiments used in this study, soil types and soil parameter values were switched back to those used in LM3.0, which we find better simulate the observed sensitivity of $V_{d,O3}$ to drought (not shown). In section 3, we evaluate how the changes in vegetation properties from LM3.0 to LM4.0 influence simulated $V_{d,O3}$.

Ozone deposition in the models is parameterized following an electrical circuit analogy as described in detail by Paulot et al. (2018).

$$V_{d,O3} = (R_a + R_b + R_c)^{-1} \qquad (1)$$

Nonstomatal resistance for O_3, which includes in-canopy aerodynamic, cuticular, stem, and ground resistances, is parameterized as a function of friction velocity, LAI, and canopy wetness (Paulot et al., 2018). In this study, the input parameters for nonstomatal deposition are modified to simulate more realistic $V_{d,O3}$ and surface O_3 over snow cover landscapes and under cold temperatures (see supporting information Text S1 and Figures S1 and S2). The updates implemented by Clifton (2018) are not included here. For stomatal deposition, we incorporate leaf physiology by combining models of stomatal behavior and photosynthesis, as an alternative approach to modeling stomatal behavior only in terms of physical variables with a Jarvis (1976)-type function. The equations for photosynthesis and stomatal conductance are described in detail in Appendices B3 and B4 of Weng et al. (2015) and are briefly summarized here.

Non–water-limited stomatal conductance $\bar{g}_s$ (mol $H_2O\cdot m^{-2}\cdot s^{-1}$) averaged over the entire canopy depth is calculated as follows:

$$\bar{g}_s = \max\left(\frac{mA^-_n}{(C_i - \Gamma_*)(1 + D_s/D_0)}, g_{s,\min}\right) \qquad (2)$$

where $\overline{A}_n$ is the net photosynthesis rate (mol $CO_2\cdot m^{-2}\cdot s^{-1}$) for a well-watered plant averaged over the entire canopy depth, m is an empirical coefficient which represents the species-specific sensitivity of stomatal conductance to photosynthesis, D_s is canopy air water vapor deficit (kg H_2O/kg air, D_0 is a reference value), C_i is intercellular concentration of CO_2 (mol CO_2/mol air), Γ_* is the CO_2 compensation point (mol CO_2/mol air), and $g_{s,\min} = 0.01$
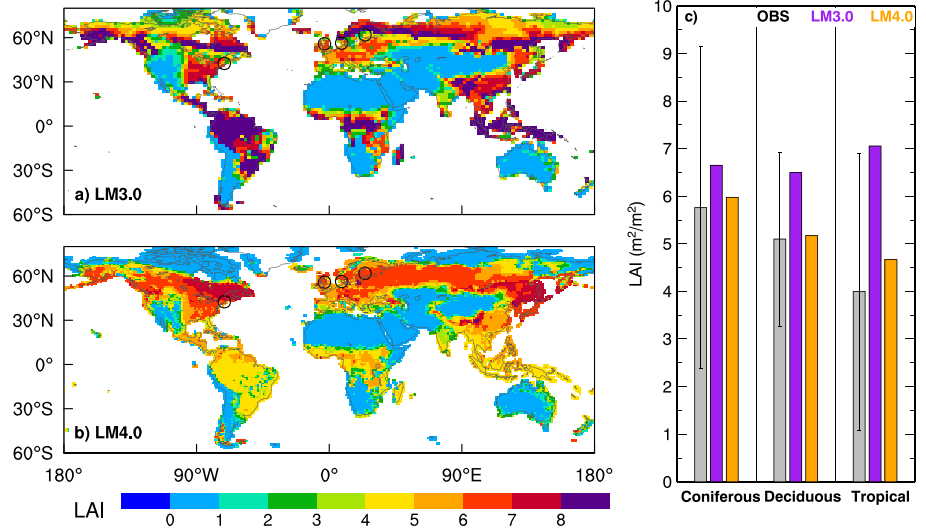
Figure 1. (a and b) Maps of June-July-August average leaf area index (LAI; 1990–2014) for natural forests in Geophysical Fluid Dynamics Laboratory LM3.0 and LM4.0. The black circles denote locations of ozone deposition velocity ($V_{d,O3}$) measurement sites at Hyytiala, Finland; Auchencorth Moss, Scotland; Ulborg, Denmark; and Harvard Forest, USA (see Figures 2 and 3). (c) Comparisons of LAI for evergreen coniferous forest, deciduous broadleaf forest, and evergreen tropical forest derived from field-based measurements (Iio & Ito, 2014) with model results.

mol $H_2O \cdot m^{-2} \cdot s^{-1}$ is the minimum stomatal conductance for water vapor allowed in the model. Increasing atmospheric water vapor deficits and CO_2 concentrations both cause $\overline{g}_s$ to decrease. A thermal inhibition factor $f(T)$ is applied to photosynthesis, affecting carbon acquisition and respiration equally:

$$f(T) = \left(1 + e^{0.4(T_1 - T_v)}\right)^{-1} \left(1 + e^{0.4(T_v - T_2)}\right)^{-1} \tag{3}$$

where T_v is leaf temperature and $T_1 = 5\,°C, T_2 = 45\,°C$. This factor causes stomatal conductance to decrease rapidly when temperature is outside of the $[T_1, T_2]$ range.

After the non–water-limited photosynthesis and stomatal conductance are determined, the model applies corrections to account for limitations imposed by soil water availability (ψ_w) and by canopy wetness (ψ_i):

$$\overline{\overline{g}_s} = \psi_w \psi_i \overline{g}_s \psi_w = \min(U_{max}/U_d 1)$$

where U_{max} is the maximum plant water uptake rate ("water supply"), defined as the uptake rate when root water potential is at the plant permanent wilting point, and U_d is "water demand," calculated as transpiration rate at non–water-limited stomatal conductance. Calculation of vegetation water uptake (Milly et al., 2014; Weng et al., 2015) takes into account the vertical distribution of soil water, the vertical distribution of fine roots, and their biomass simulated by the LM3.0/LM4.0 vegetation dynamics (Shevliakova et al., 2009). In each soil layer, roots are represented as cylinders of small radius, and the difference between bulk water potential of the soil and water potential at the soil-root interface for this layer is determined by the near-field steady-state solution of the flow equation (Gardner, 1960), with xylem of the plant-root system providing the connection across layers (Weng et al., 2015).

Downregulation of photosynthesis due to water interception is

$$\psi_i = 1 - (f_s + f_l)\alpha_{wet}$$

where f_s and f_l are the fractions of canopy covered by snow and liquid water, respectively; α_{wet} is the downregulation coefficient, assumed to be 0.3 (i.e., photosynthesis of leaves fully covered by water or snow is reduced by 30% compared to dry leaves).
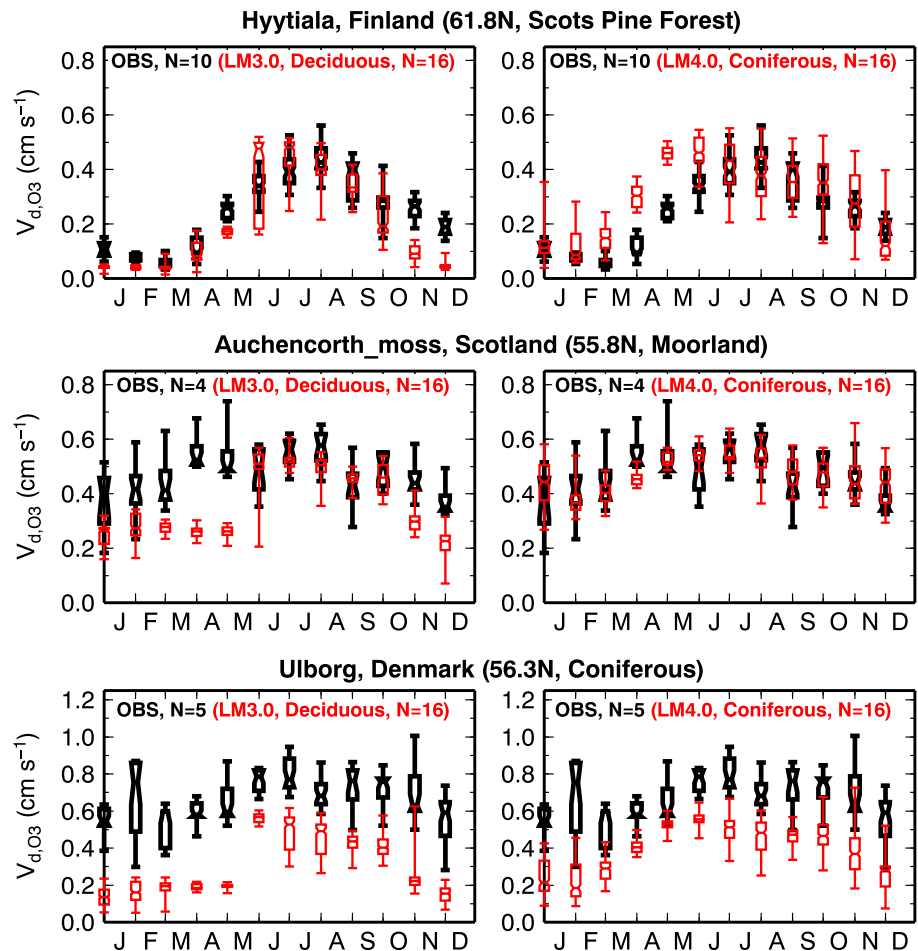
Figure 2. Comparisons of monthly 24-hr mean V_{d,O_3} at north European forest sites as observed (black) and simulated (red) by Geophysical Fluid Dynamics Laboratory LM3.0 (left column) and LM4.0 (right column). Here and in other figures, the box-and-whisker plots give the minimum, 25th to 75th percentiles, and maximum of monthly average values over the measurement periods (Table 1) and for the model period 1995–2010. N indicates the number of years.

We conduct a suite of approximately 600-year simulations with LM3.0 and LM4.0. The experiments consist of a 300-year potential vegetation spin-up phase (undisturbed by human activity), an intermediate land use spin-up phase (1700–1860; Hurtt et al., 2011), and a historical phase (1861–2014) with varying CO_2 and land use (see Text S2). The dry deposition simulations are initialized from the 1948 conditions in the historical phase and continue through 2014, driven by observation-based meteorological forcings (Sheffield et al., 2006; 3-hourly precipitation, humidity, pressure, downward short and longwave radiation, and near-surface temperatures and winds; available at http://hydrology.princeton.edu/data.php). These stand-alone land model hindcast simulations driven by observationally based atmospheric forcings (here after "LM3.0" or "LM4.0") allow us to first investigate uncertainties in V_{d,O_3} parameterizations. Then we couple the land model to an atmospheric model ("AM3_LM3"; starting from the same 1948 initial land conditions as in LM3.0) to investigate the influence on simulated V_{d,O_3} from uncertainties in model atmospheric forcings, particularly precipitation (section 4). To examine the influence of changes in V_{d,O_3} on surface O_3, we also conduct a simulation with a prototype version of the new GFDL AM4 chemistry-climate model using prescribed V_{d,O_3} archived hourly from the stand-alone LM4.0 simulation ("AM4_LM4dd"; section 6).

3. Factors Controlling Seasonal Cycle of Ozone Deposition Velocity

In this section, we discuss the simulation of vegetation properties that strongly influence the seasonality of O_3 dry deposition. We discuss relevant improvements in the parameterization of these properties from LM3.0 to LM4.0 and show how these changes improve the simulation of V_{d,O_3}.
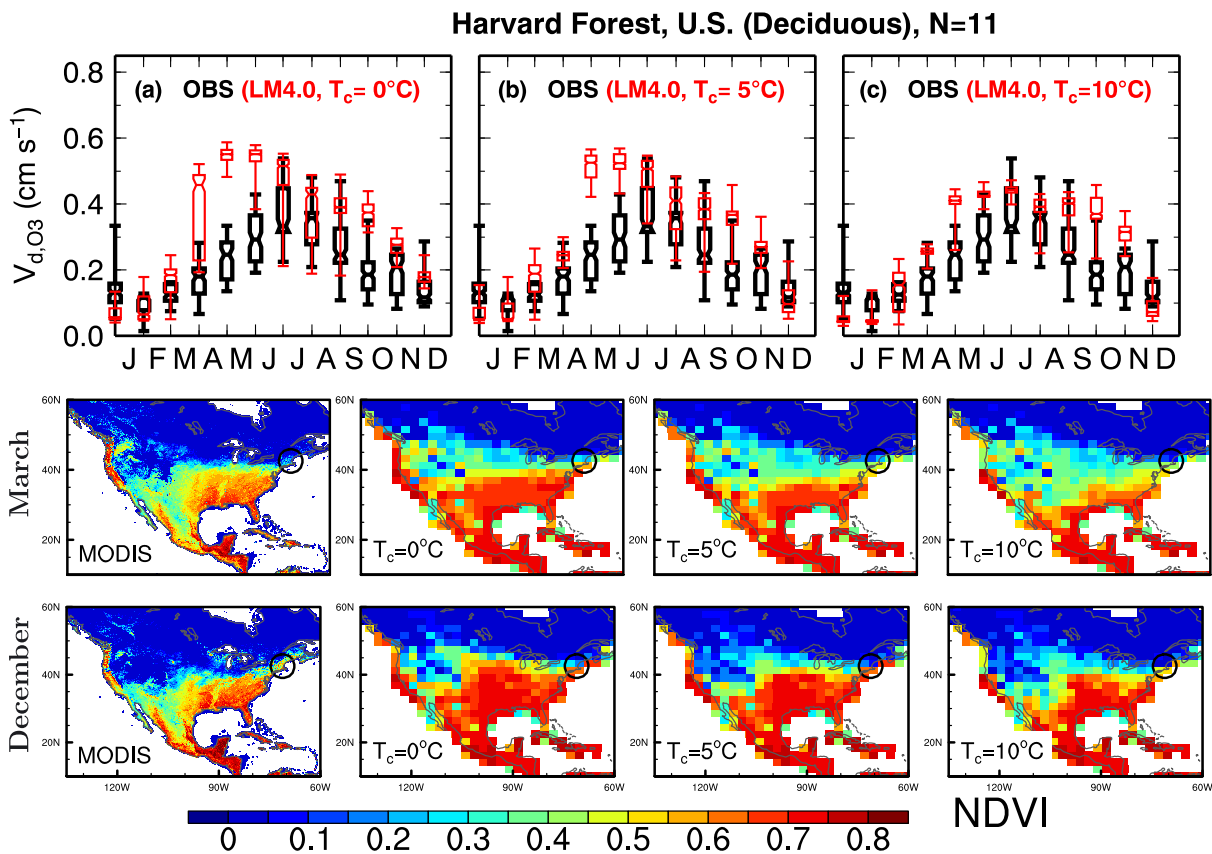
Figure 3. (top row: a–c) Monthly 24-hr mean V_{d,O_3} at Harvard Forest from observations and LM4.0 simulations with different T_c for deciduous forests. (bottom row) Maps of March and December normalized difference vegetation index (NDVI) over North America for Moderate Resolution Imaging Spectroradiometer (MODIS) and LM4.0 with different T_c, averaged over the 2001–2006 MODIS observation period. NDVI is computed for each month as the difference between surface near-infrared and visible reflectances, divided by their sum. The black circles denote the location of Harvard Forest.

3.1. Distribution of Vegetation Types

Figure 1 shows comparisons of JJA average LAI for natural forests in LM3.0, LM4.0, and field-based measurements. The observational data set is a compilation of field-observed data for woody species at 1,216 locations, obtained from 554 literature sources published between 1932 and 2011 (Iio & Ito, 2014). LM4.0 better simulates the LAI values for cold evergreen forest, deciduous forest, and tropical forest, while LM3.0 overestimates the field-based data, particularly for the deciduous and tropical forests. The improved simulation of LAI in LM4.0 reflects the new parameterization of light limitation on the maximum attainable LAI. In this parameterization, if the light level at the bottom of the canopy is so low that the leaves cannot support their own physiological demands, the lifetime of these leaves is reduced.

In addition to the differences in LAI values, the two models also differ in the cold evergreen-temperate deciduous forest boundary (depicted as sharp LAI gradients around 40–60°N in Figure 1a vs. Figure 1b). The cold evergreen tree type is assigned when the number of cold months (average canopy air temperature below 10 °C) is in the range 9–12 for LM3.0 but 7–9 for LM4.0. The change was made to better locate the region of cold evergreen forest, as reflected in MODIS reflectance observations (Milly et al., 2014). The change in the cold evergreen-temperate deciduous forest boundary from LM3.0 to LM4.0 affects the simulated seasonality of V_{d,O_3} in these areas, as illustrated in Figure 2 for three northern European forest sites. LAI is a primary driver of the observed seasonality in V_{d,O_3} at a moorland site in Auchencorth Moss, Scotland, and a mixed coniferous forest at Ulborg, Denmark (Fowler et al., 2001; Mikkelsen et al., 2004). At the far northern Hyytiala coniferous forest site, the dormancy of vegetation, below-zero temperatures, and snow cover result in low and relatively stable observed V_{d,O_3} in winter (Rannik et al., 2012). These sites are located in temperate deciduous forest areas in LM3.0; thus, both the interannual spread and magnitude of wintertime V_{d,O_3} are
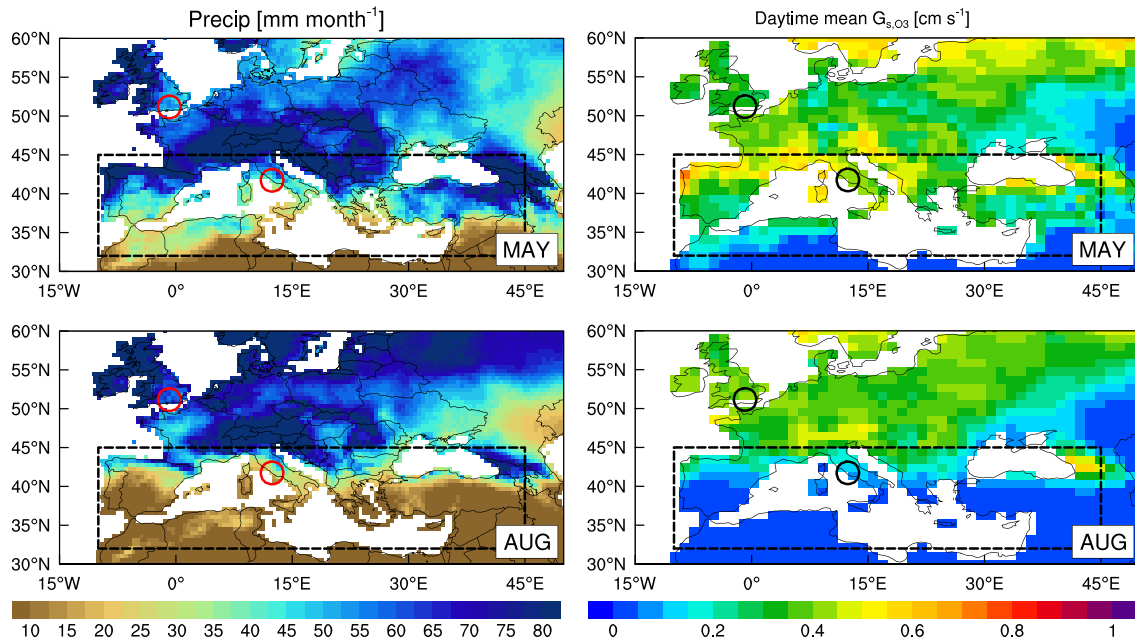
Figure 4. Maps of observed precipitation and LM4.0 simulated daytime (9 a.m. to 3 p.m.) mean stomatal conductance for O_3 ($G_{s,O3}$, averaged over four land use categories) over Europe in May versus August over 1990–2014. The red circles denote the locations of holm oak forests at Alice Holt, England, and Castelporziano, Italy (see Figure 5).

underestimated, due to a lack of wintertime LAI. In contrast, LM4.0 better captures the observed seasonality of $V_{d,O3}$ at these sites (though some biases remain, e.g., too large springtime $V_{d,O3}$ at Hyytiala). For the growing season, both models simulate lower $V_{d,O3}$ than observed at Ulborg. This discrepancy may reflect uncertainties in $V_{d,O3}$ measurements derived from the gradient method, which in general are greater than those obtained with the eddy correlation method (Wu et al., 2015).

3.2. Critical Leaf Temperature

Figure 3 illustrates the influence of changes in critical leaf temperature (T_c) on seasonality of simulated $V_{d,O3}$ at a temperate deciduous forest. Cold triggering of leaf drop in LM3.0 occurs at 5 °C for C3 grass and 10 °C for other vegetation types (Shevliakova et al., 2009). In the standard version of LM4.0, T_c is set to 0 °C for all vegetation types, but we find that the model overestimates observed LAI and $V_{d,O3}$ in spring at Harvard Forest. Thus, we conduct a suite of LM4.0 sensitivity simulations with T_c for deciduous trees set to 0, 5, and 10 °C, respectively, and examine the modeled seasonal green-up in midlatitude regions as compared to MODIS normalized difference vegetation index (NDVI) observations. With T_c set to 10 °C, the modeled NDVI at Harvard Forest in March agrees well with MODIS data, consistent with the better agreement in $V_{d,O3}$ at the site compared with the T_c = 0 °C simulation, but the green-up in the central eastern United States occurs too late. With T_c = 0 °C the modeled NDVI above 40°N is too high in December, indicating that deciduous trees in that area do not drop leaves realistically. Overall, the simulation with T_c set to 5 °C best matches the seasonal cycle of green leaf area inferred from satellite data over North America and other mid-latitude regions, although it still overestimates $V_{d,O3}$ in May observed at Harvard Forest. Based on our evaluation, we adopt T_c = 5 °C for deciduous trees and C4 grass in the LM4.0 simulations with interactive dry deposition. T_c for the other vegetation types are set to 0 °C as in LM3.1 (Milly et al., 2014). Changes in T_c modulate the growth cycle of vegetation and thus can also influence simulated LAI values and interannual variability of $V_{d,O3}$ in summer.

3.3. Water Availability

We next examine the influence of spatial and seasonal variations of water availability on stomatal conductance and $V_{d,O3}$, by contrasting sites in southern Europe with a Mediterranean climate and those in northern Europe with a wet summer. Located on the western coasts of Europe (roughly between 35°N to 45°N), a Mediterranean climate is characterized by rainy winters and springs but dry summers (Figure 4). In May,
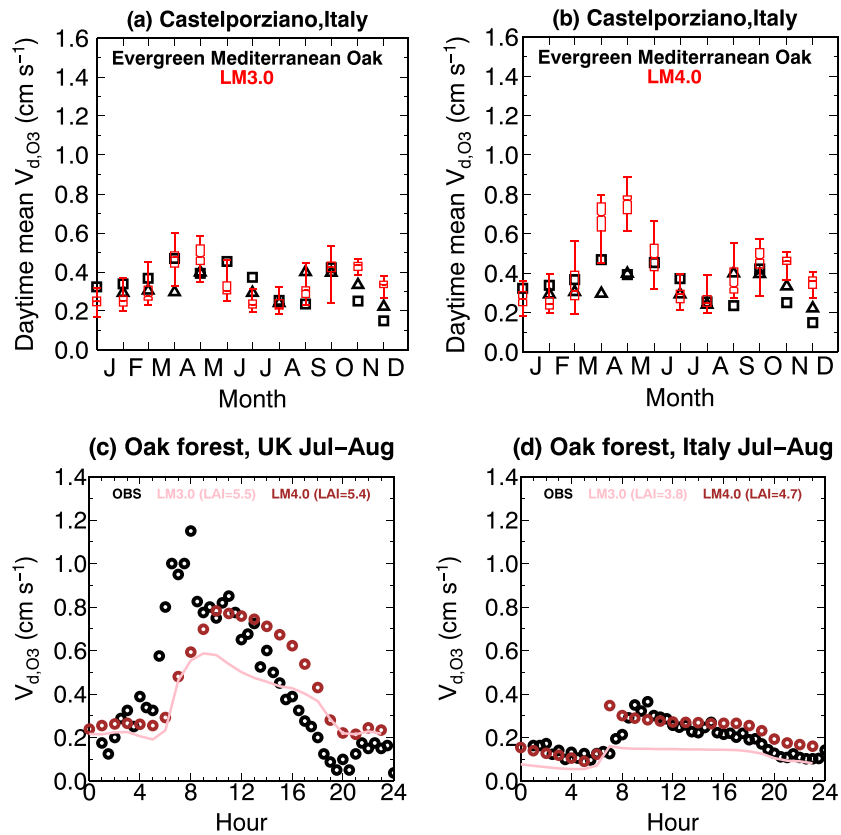
Figure 5. (a, b) Monthly daytime (9 a.m. to 3 p.m.) mean $V_{d,O3}$ at Holm oak forest, Castelporziano, Italy, derived from observations (2012–2013) and Geophysical Fluid Dynamics Laboratory land model simulations (1990–2013). (c, d) July–August mean diurnal cycle of $V_{d,O3}$ at holm oak forests in Alice Holt, England, versus Castelporziano, Italy.

with plentiful precipitation throughout Europe, LM4.0 simulates a daytime mean (9 a.m. to 3 p.m.) O_3 stomatal deposition rate ($G_{s,O3}$) of 0.4 to 0.6 cm/s. The $G_{s,O3}$ values decrease to below 0.2 cm/s in Mediterranean Europe during August with dry conditions. The modeled spring to summer $G_{s,O3}$ decreases are consistent with measurements from a typical Mediterranean maquis ecosystem in Italy during May versus July of 2007 (Gerosa, Finco, Mereu, Marzuoli, & Ballarin-Denti, 2009; Rydsaa et al., 2016). Simultaneous measurements of water vapor and O_3 fluxes at an evergreen Holm Oak forest at Castelporziano, Italy, indicate that stomatal pathways explained almost the totality of O_3 fluxes during winter but less than 50% in daytime during summer under condition of drought stress (Fares et al., 2014).

Figures 5a and 5b compare monthly daytime mean $V_{d,O3}$ at Castelporziano from observations and GFDL land model simulations. Both LM3.0 and LM4.0 capture the observed decreases in $V_{d,O3}$ from April to August at the Mediterranean Oak Forest, driven by the reduced efficiency of stomatal deposition under drought stress, with LM4.0 simulating higher $V_{d,O3}$ in April–May. Water availability also influences the spatial variability of $V_{d,O3}$ in northern Europe versus southern Europe during late summer. For example, Figures 5c and 5d compare July–August mean diurnal cycle of $V_{d,O3}$ at Castelporziano versus over a holm oak forest at Alice Holt, England (Fowler et al., 2009). Observed July–August daytime mean $V_{d,O3}$ is 0.6–1.2 cm/s at Alice Holt but decreases to 0.2–0.3 cm/s at Castelporziano. LM4.0 generally reproduces the observed $V_{d,O3}$ variability between the two sites and attributes it to large-scale decreases in stomatal conductance associated with water stress in the southern European forest during late summer (Figure 4). Note that changes in LAI are not the major driver of the modeled $V_{d,O3}$ variability between the sites. Large vapor pressure deficits, especially in the Mediterranean region, may also lead to limitation of stomatal conductance. Such an effect has been previously observed for water-saving tree species such as Holm Oak (Quercus ilex), which tend to close their stomata to prevent severe water losses (Manes et al., 2007; Mereu et al., 2009). This phenomenon is often associated with drought conditions; it is therefore not easy to disentangle single effects.
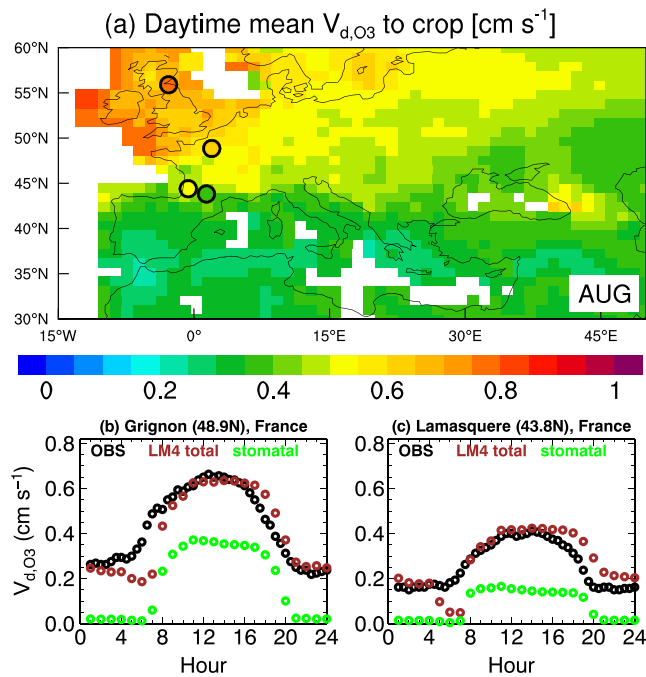
Figure 6. (a) Map of August daytime mean V_{d,O_3} to croplands over Europe in Geophysical Fluid Dynamics Laboratory-LM4.0 (1990–2014). The color-filled circles denote observations at potatoes, Gilchriston, Scotland (Coyle et al., 2009), and three maize crop sites in France (Stella et al., 2011). (b) Comparisons of observed and modeled diurnal cycle of V_{d,O_3} at maize crops in Grignon, France, July–August 2008. Both total (brown) and stomatal (green) deposition from LM4.0 are shown. (c) Same as (b) but for Lamasquere in a Mediterranean climate.

For croplands over Europe (Figure 6a), LM4.0 simulates higher late summer V_{d,O_3} values in the north, consistent with the spatial patterns of precipitation and stomatal conductance (Figure 4). Interestingly, the simulated north-to-south gradient in daytime mean V_{d,O_3} to croplands mimics the V_{d,O_3} variations inferred from O_3 eddy covariance measurements at a potato field in Scotland (Coyle et al., 2009) and three maize crop sites in France (Stella et al., 2011; color filled circles in Figure 6a). Sampling LM4.0 at Grignon in northern France with plentiful precipitation and at Lamasquere in a dry Mediterranean climate indicates that reduction of stomatal deposition during daytime can explain the changes in total V_{d,O_3} at the two sites (Figures 6b and 6c). For Lamasquere, the observed low LAI (Table 1) likely contributes to lower observed V_{d,O_3}, although the modeled LAI does not show much difference at the sites (Figure S3). During daytime at Grignon, the stomatal pathway represents half of the total deposition in the model, consistent with that inferred from water vapor flux measurements at Grignon when maize was fully developed (Stella et al., 2011). The model slightly underestimates daytime V_{d,O_3} at the Gilchriston potato field in Scotland (0.7 cm/s in the model compared to 0.8 cm/s deduced from observations; Figure 6a). One possible explanation is an underestimate of enhanced nonstomatal deposition to a wet canopy surface, which Coyle et al. (2009) suggested was an important process at the Gilchriston site.

Seasonal water availability is also found to affect stomatal conductance and total V_{d,O_3} in evergreen tropical forests over Amazon and South Asia (Figure 7). Short-term (10–20 days) observations in the Amazon rainforest show that daytime mean V_{d,O_3} decreases from 1.1–1.8 cm/s in the wet season (February-March-April) to only 0.5 cm/s in the dry season (JJA; filled circles in Figure 7a; Fan et al., 1990; Rummel et al., 2007). LM4.0 captures the observed anomalies, with simulated V_{d,O_3} in the southeast parts of the Amazon rainforest decreasing from 0.7–0.8 cm/s in the wet season to 0.2–0.3 cm/s in the dry season (Figure 7a). Mean V_{d,O_3} magnitude over Amazon in the model is generally smaller than observations. While the source of this problem is unclear, it may reflect some combined influence from differences in the scales of observations and model simulations, errors in the atmospheric forcings, the uncertainty in the model's parameters and structure, and the uncertainty in the flux measurements themselves. Over South Asia, observed daytime mean V_{d,O_3} above a tropical forest in Thailand is 0.6 cm/s in the wet season (JJA) compared to 0.3 cm/s in the dry (February-March-April) season (Matsuda et al., 2005; Matsuda et al., 2006), consistent with LM4.0 simulations (Figure 7b). The seasonality of V_{d,O_3} in these tropical forests is primarily driven by the seasonality of regional precipitation that affects stomatal conductance through changes in soil moisture (Figure S4). The seasonal changes in LAI are small for most areas (Figure S5). The model indicates that O_3 uptake by tropical forest in India is also susceptible to drought effects in the dry season. Over the rainforest in Malaysia and Indonesia, for comparison, the lack of seasonality in rainfall leads to year-round active O_3 uptake, with simulated daytime mean V_{d,O_3} ranging from 0.7–0.9 cm/s (Figure 7b), close to the observed value of 0.9 cm/s from a rainforest in Borneo during July 2008 (filled circles in Figure 7b, data from Fowler et al., 2011).

4. Interannual Variability of Ozone Deposition Velocity

4.1. Observed Reduction of Ozone Deposition to Forest Under Drought

Ozone concentrations and fluxes have been measured continuously during 1995–2000 by a gradient method at a Norway spruce-dominated forest at Ulborg, Denmark (Mikkelsen et al., 2004). The data are analyzed here to examine interannual variability of V_{d,O_3} and its relationship to large-scale drought in northern Europe. We calculate 5 years of half-hourly V_{d,O_3} from O_3 concentrations and flux measurements at 18–36 m above the ground. Similar to the approach used in Clifton et al. (2017) for Harvard Forest, we remove outliers by rejecting any half-
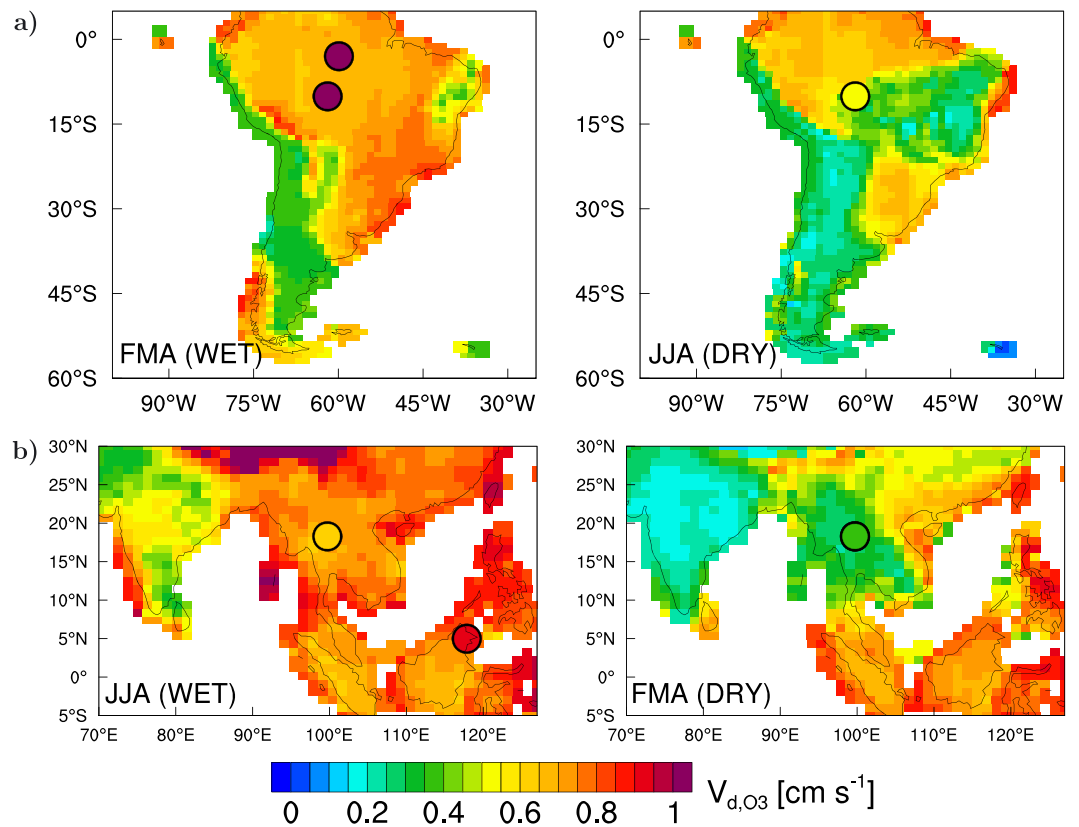
Figure 7. Influence of water availability on $V_{d,O3}$ during the wet and dry seasons for evergreen tropical forests in (a) Amazon and (b) South Asia. Shown are observed daytime mean $V_{d,O3}$ at measurement sites (color-filled circles; see also Table 1) superimposed on maps of LM4.0 $V_{d,O3}$ simulations averaged over 1990–2014.

hourly $V_{d,O3}$ values falling outside ± 5 standard deviations of the half-hourly time series during May–September. Figure 8a shows the time series of the monthly daytime mean (9 a.m. to 3 p.m.) $V_{d,O3}$ at Ulborg from 1995 to 2000, with drought events indicated. Drought events are defined using the Standardized Precipitation-Evapotranspiration Index (SPEI; Begueria et al., 2014), calculated using monthly precipitation and potential evapotranspiration from the Climate Research Unit data set (Harris et al., 2014). SPEI can be calculated over a variable integration time scale (e.g., SPEI06, 6-month SPEI, integrates water status over the previous 6 months), with more negative values indicating more severe drought relative to long-term average conditions. We use SPEI06 < -1 as the threshold for a drought event to calculate the percentage area in drought over a specific region: for instance, northern Europe (50–65°N, 10°W to 30°E), for the purpose of investigating large-scale climate conditions influencing $V_{d,O3}$ variability at Ulborg. Monthly daytime mean $V_{d,O3}$ at Ulborg are lowest in 1995–1996 during a severe, prolonged drought in Denmark (Figure 8b). In contrast, observed daytime mean $V_{d,O3}$ are highest in 1998 when persistent rainfall across northern Europe maintained sufficient soil moisture (Figure 8c). Using a bootstrap technique, we find that the highest and lowest daytime mean $V_{d,O3}$ values in each month are significantly different between 1996 and 1998 at a 95% confidence level.

Figure 9 further demonstrates reduced $V_{d,O3}$ to North American deciduous forests under conditions of large-scale drought stress. Dry deposition of O_3 is derived from gradient measurements at Borden Forest in southern Ontario, Canada, from May 2008 to April 2013 (Wu et al., 2016). The 5-year measurements at Borden Forest include the 2012 North American drought, with its peak occurred during a record-breaking heat wave in late June to July. The drought covered most of the United States and Eastern Canada, including southern Ontario. Our analysis shows that daytime mean $V_{d,O3}$ at Borden Forest decreases by ~0.40 cm/s in observations and ~0.45 cm/s in the model during the dry and hot July of 2012 relative to the wet and cool July of 2009 (Figures 9a–9d). Supporting the conclusion drawn from sparse gradient measurements, LM4.0 indicates that the drought-induced $V_{d,O3}$ decreases in 2012 were widespread across eastern North America (Figures 9e and 9f). The model shows little change (<1) in LAI between the two summers (Figure S6). The limitation of
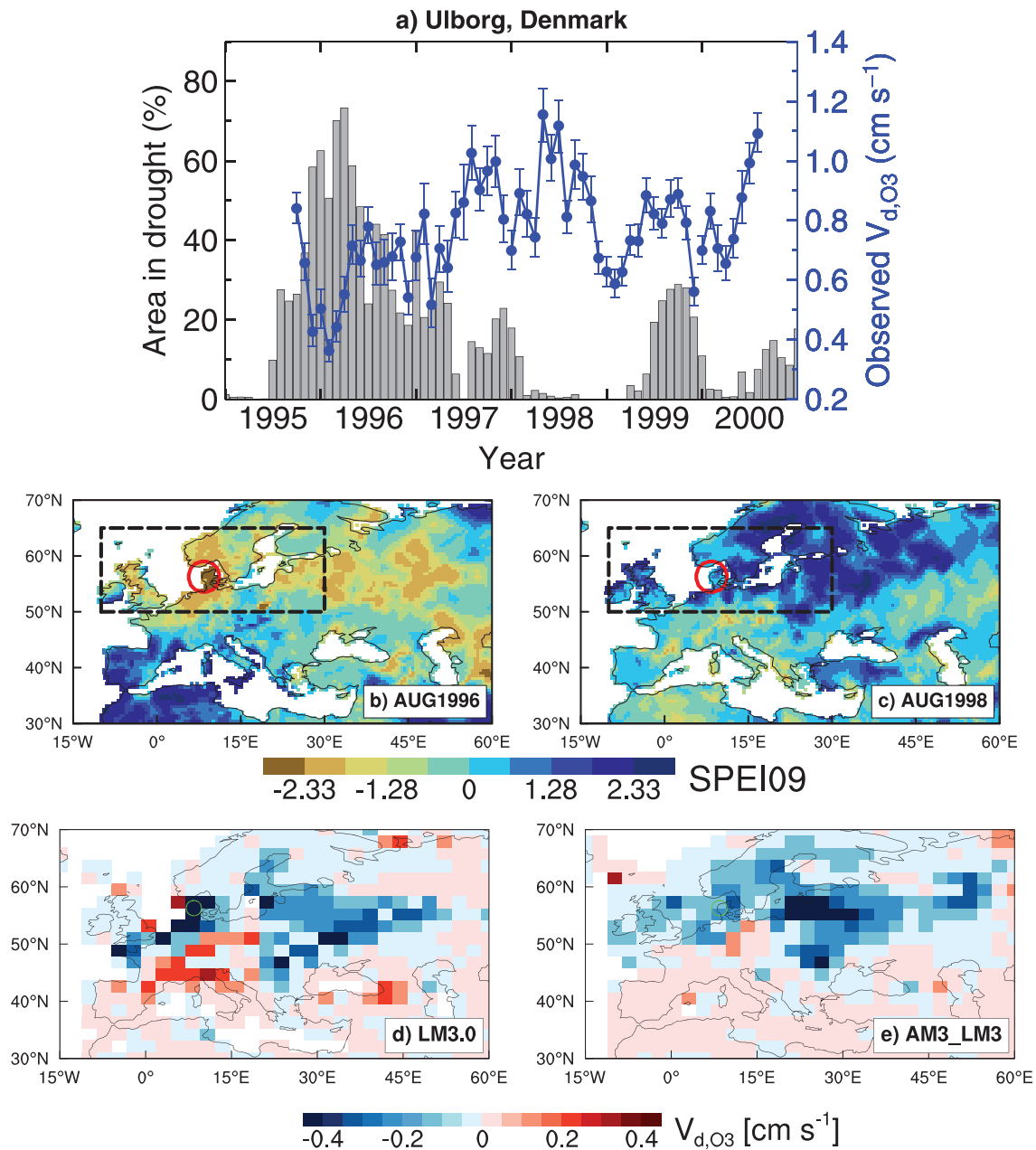
Figure 8. (a) Time series of area in drought (SPEI06 < -1.0) over northern Europe (gray bars; box on map) and monthly daytime (9 a.m. to 3 p.m.) mean $V_{d,O3}$ from observations at Ulborg, Denmark (blue symbols; right axis), from 1995 to 2000. Error bars in $V_{d,O3}$ indicate 95% confidence intervals estimated with a bootstrapping technique (https://www.ncl.ucar.edu/Document/Functions/Bootstrap/bootstrap_stat.shtml). (b and c) Maps of 9-month (February–August) SPEI drought index over Europe for 1996 versus 1998. The 9-month SPEI (as opposed to the 6-month SPEI) is shown to highlight the prolonged feature of the 1995–1996 drought. (d and e) Anomalies in July–August daytime mean $V_{d,O3}$ for 1996 relative to 1998 from LM3.0 driven by observation-based meteorological forcings versus coupled with AM3 nudged to the reanalysis winds. Circles denote the location of Ulborg. SPEI = Standardized Precipitation-Evapotranspiration Index.

stomatal conductance associated with soil drying is the primary driver of simulated $V_{d,O3}$ decreases during such large-scale midlatitude droughts. The reduced O_3 uptake by vegetation exacerbated the buildup of surface O_3 levels to 75–135 ppbv (8-hr average) at monitoring stations across the central and eastern United States during the 2012 heat wave and drought.

4.2. Influence of Model Precipitation Biases

We next examine the influence of uncertainties in model precipitation on $V_{d,O3}$ means and extremes, recognizing that precipitation is the main driver of variability in drought and stomatal conductance.
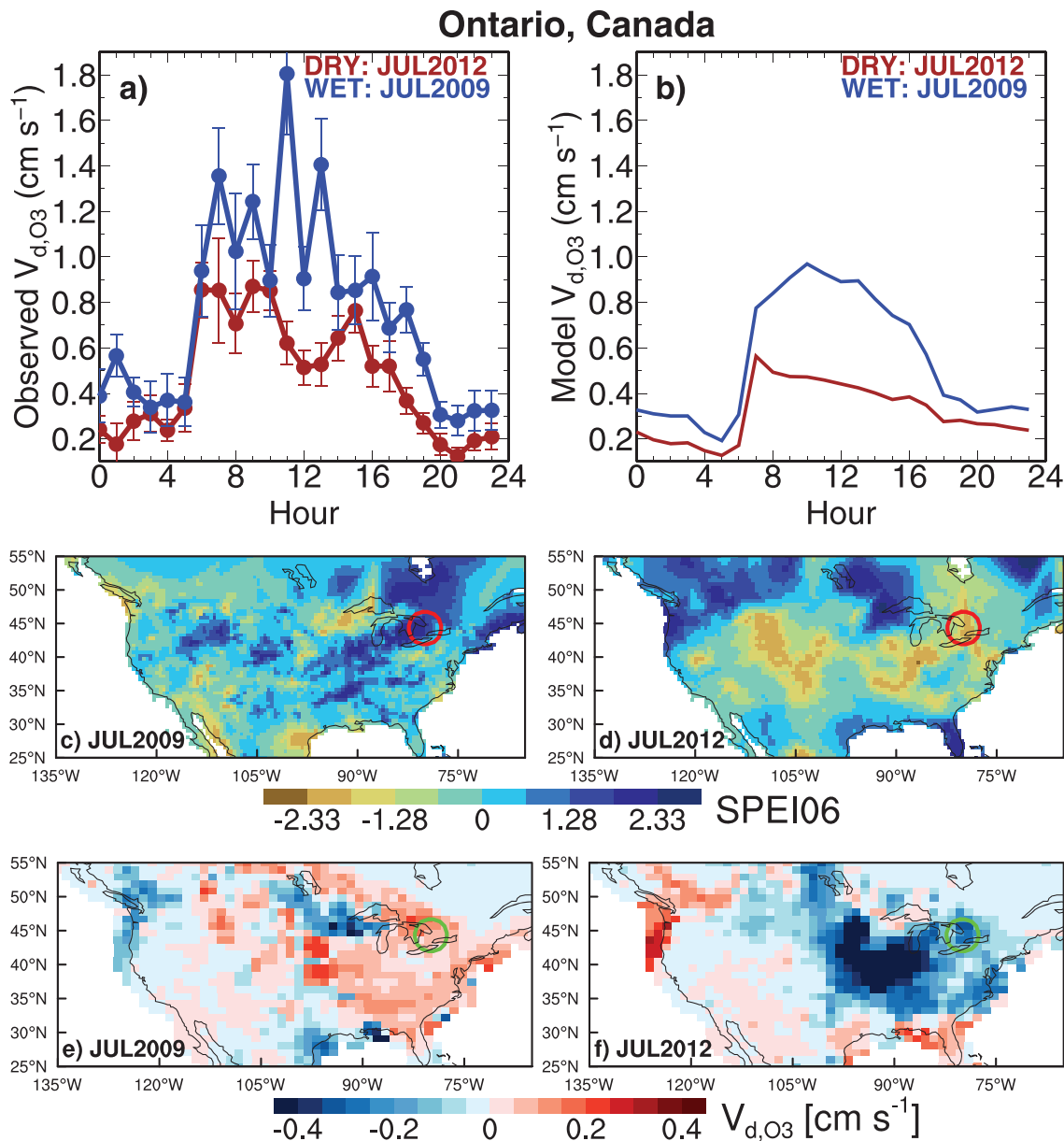
Figure 9. (a and b) Diurnal cycle of $V_{d,O3}$ at Borden Forest, Ontario, Canada, in July 2009 (wet) versus July 2012 (dry) derived from observations (±s.d.) and from LM4.0 simulations. (c and d) Maps of 6-month (February–July) Standardized Precipitation-Evapotranspiration Index (SPEI) for 2009 versus 2012. and f) Maps of LM4.0 simulated anomalies (relative to 1990–2014 mean) in daytime $V_{d,O3}$ over forests for July 2009 and 2012. Circles on map denote the location of Borden Forest.

Using Europe as an example, we contrast regional $V_{d,O3}$ variability simulated in LM3.0 driven by the observation-based meteorological forcings (including precipitation) versus LM3.0 coupled with the GFDL Atmospheric Model Version 3 (hereafter AM3_LM3). AM3_LM3 is nudged to National Centers for Environmental Prediction horizontal winds using a pressure-dependent nudging technique (Lin et al., 2012; Lin et al., 2015), while precipitation is simulated internally by the model. Figure 8d shows that stand-alone LM3.0 simulates $V_{d,O3}$ decreases in northern Europe and increases in southern Europe in July–August 1996 relative to 1998, consistent with the dry versus wet forested areas inferred from SPEI. Stand-alone LM3.0 simulates $V_{d,O3}$ anomalies at Ulborg (~0.4 cm/s) that are comparable to the observed values. In contrast, $V_{d,O3}$ anomalies at Ulborg in the coupled model AM3_LM3 are weaker by a factor of 2 than observed, with no systematic changes in $V_{d,O3}$ over southern Europe (Figure 8e). These biases are caused by limitations in the accurate simulation of regional rainfall and drought,
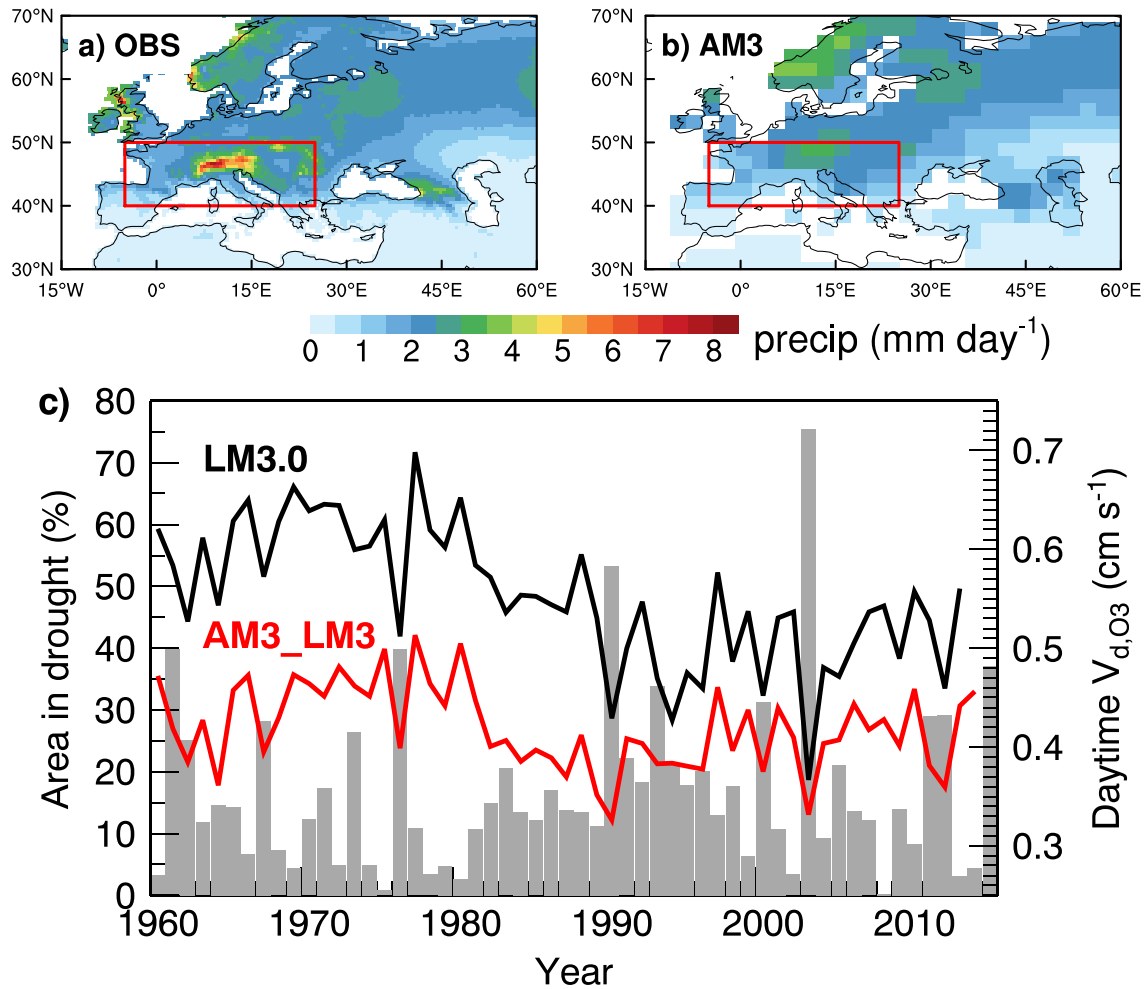
Figure 10. (a and b) June-July-August precipitation averaged over 1981–2010 from Climate Research Unit observations and AM3 simulations. (c) Time series of June-July-August daytime mean $V_{d,O3}$ to natural forests averaged over western Europe (box on map) as simulated in LM3.0 driven by observed atmospheric forcings (black) versus coupled with AM3 (red). The gray bars indicate the percentage area of western Europe in drought derived from SPEI06 (March through August).

particularly their extremes, by the model when constrained only by observed horizontal winds and sea surface temperatures.

AM3 underestimates precipitation in southern Europe (Figures 10a and 10b). Given its coarse resolution (~200 × 200 km^2), the model fails to reproduce intense precipitation in the European Alps. These precipitation biases affect not only the mean of $V_{d,O3}$ but also extremes, as shown in the time series analysis of JJA daytime mean $V_{d,O3}$ to natural forests averaged over southern Europe from 1960 to 2014 (Figure 10c). In stand-alone LM3.0 driven by observed atmospheric forcings, summertime $V_{d,O3}$ over southern Europe varies strongly on interannual to decadal time scales, correlating with the drought index. Particularly, LM3.0 simulates the lowest $V_{d,O3}$ over the 55-year record during the 2003 European megadrought. In the coupled model AM3_LM3, the interannual variability of $V_{d,O3}$ is weaker by approximately a factor of 2 and the $V_{d,O3}$ decrease in summer 2003 is not the most extreme over the past half century. While we only have the long-term coupled model simulation available from AM3_LM3 with interactive dry deposition, examination of precipitation fields from AM4 with higher horizontal resolution (Zhao et al., 2018a, 2018b) still shows a similar difficulty in simulating the regional drought extremes like summer 2003. Thus, the coupled AM4_LM4 model is expected to simulate weaker $V_{d,O3}$ variability than stand-alone LM4.0.
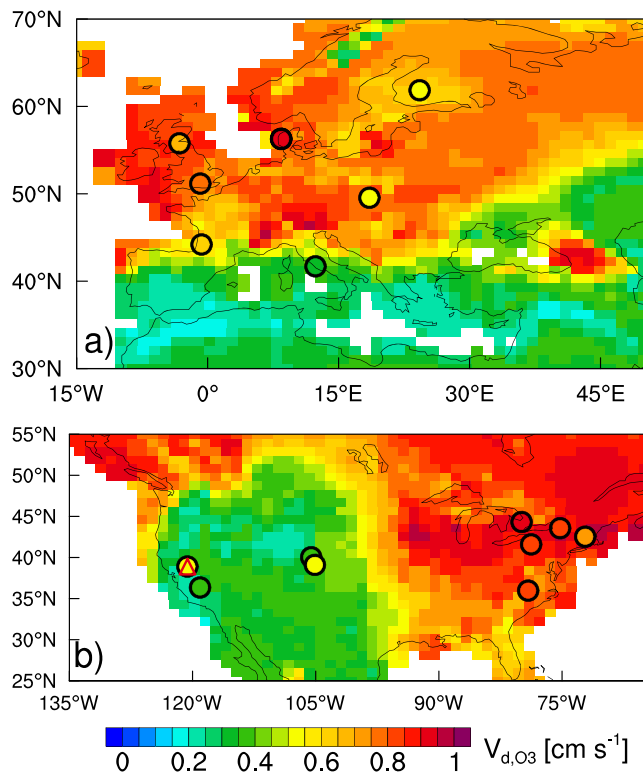
Figure 11. (a, b) June-July-August daytime mean $V_{d,O3}$ to natural forests in LM4.0 (1990–2014) over Europe and North America, with the color-filled symbols representing observed values at available sites (Table 1).

5. Global Distributions of $V_{d,O3}$ and Contributions From Stomatal Pathways

Daytime mean $V_{d,O3}$ during the warm season in LM4.0 typically ranges from 0.6 to 1.0 cm/s for natural and secondary vegetation (primarily forests), 0.4 to 0.7 cm/s for croplands, and 0.3 to 0.5 cm/s for pastures in the absence of drought (Figure S7). These values are generally consistent with observations (Table 1). We focus next on a detailed evaluation of JJA daytime mean $V_{d,O3}$ to European and North American forests, where observations are relatively dense. Drought stress and reduced stomatal uptake during late summer in the Mediterranean region (section 3.3) lead to a north-to-south contrast in observed $V_{d,O3}$, with higher $V_{d,O3}$ in northern Europe than in southern Europe (Figure 11a). Over North America, $V_{d,O3}$ generally increases from west to east (Figure 11b), driven by increases in LAI (Figure 1). The observed regional variability of $V_{d,O3}$ over Europe and North America is well simulated in LM4.0. The largest discrepancy between observations and simulations occurs at Blodgett Forest in California (small triangle in Figure 11b), where observed JJA daytime $V_{d,O3}$ is 0.92 cm/s for 2001–2007 (Fares et al., 2010) and 0.5 cm/s for 1999 (Kurpius et al., 2002), versus 0.4 cm/s in the model. Fares et al. (2010) suggested that in-canopy chemical reactions with terpenoids emitted by the ponderosa pine ecosystem at Blodgett Forest are mainly responsible for the rapid O_3 sink in their observations, whereas the deposition scheme in our model does not include the influence of in-canopy chemistry.

Figures 12a and 12b depict the 1990–2014 mean contribution of stomatal pathways to the total $V_{d,O3}$ in LM4.0 for Northern Hemisphere summer (see also Figures S8 and S9 for the global maps). Considering both nighttime and daytime conditions, stomatal pathways account for ~50% of the total $V_{d,O3}$ to natural or secondary vegetation and ~25% to croplands or pastures at northern midlatitude regions without drought disturbances. However, considering only daytime conditions, especially under optimal climatic conditions (e.g., plentiful precipitation) for plant functioning, stomatal pathways represent up to 75% of the total $V_{d,O3}$ for natural or secondary vegetation, 40% for croplands, and 35% for pastures. In the dry Mediterranean climate, the daytime contributions of stomatal deposition decrease by almost a factor of 2 compared to the other regions that do not typically experience late summer droughts (Figure 12a). These model estimates of $V_{d,O3}$ stomatal fraction are close to the sparse observation-based estimates from scaling eddy covariance measurements of water vapor or CO_2 fluxes. The summer daytime (9 a.m. to 3 p.m.) stomatal fraction estimated from observations is 41–82% (multiyear mean is 59%) at Harvard Forest for 1990–2000 (Clifton et al., 2017) and 65% at Kane Experiment Site for 1997 in the eastern United States (Zhang et al., 2006). Over Europe, estimates are 65–80% at an oak forest in England for 2005 (Coyle et al., 2006), 60% at a boreal pine forest in Finland for 2001–2010 (Rannik et al., 2012), and <50% at a Mediterranean oak forest in Italy for 2003–2014 and 2012–2013 (Fares et al., 2014; Gerosa, Finco, Mereu, Vitale, et al., 2009). Note that the observation-derived stomatal O_3 fluxes suffer from uncertainties due to the inversion of Penman-Monteith equation used to calculate stomatal conductance from evapotranspiration, particularly at sites where the evaporative component of water fluxes is not negligible (Fares et al., 2018).

Figures 12c and 12d illustrate the interannual variability in JJA daytime mean $V_{d,O3}$ for natural forests in LM4.0, expressed as the relative standard deviation (ratio of the standard deviation to the mean) and the ratio of maximum to minimum values across 35 years from 1980 to 2014. The model indicates that semiarid areas of western Europe, eastern North America, and northeastern China have the largest interannual variability in $V_{d,O3}$, with the relative standard deviation ranging from 15% to 35%. Over these regions, summertime mean $V_{d,O3}$ for the highest year can be a factor of 2 to 4 higher than that for the lowest, with significant implications for surface O_3 interannual variability.
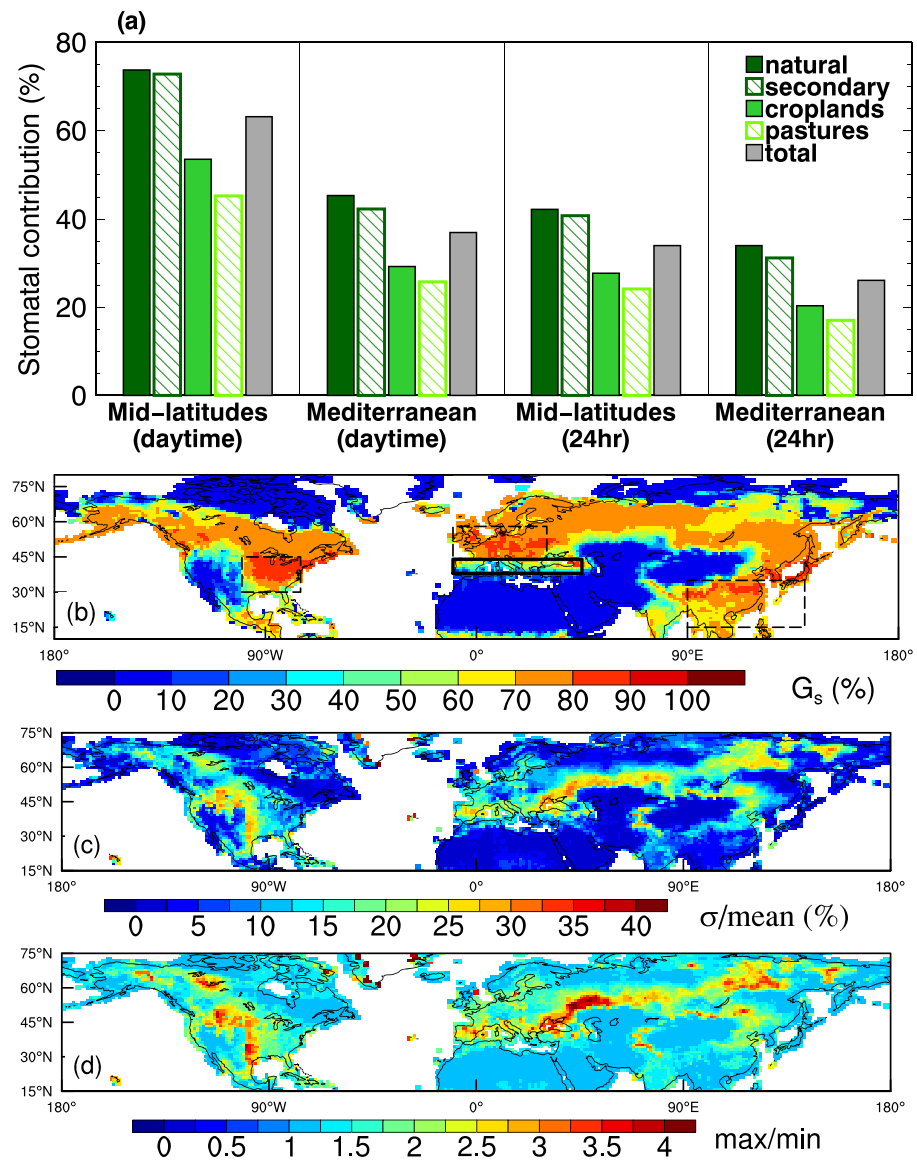
Figure 12. (a) The 1990–2014 mean stomatal fraction to the total deposition at four land use categories in LM4.0 for June-July-August (JJA) daytime and 24-hr means, respectively, over northern midlatitude regions (dashed boxes on map) versus over the semiarid Mediterranean region (solid box). (b) Map of the JJA daytime mean stomatal fraction for forests (see Text S3 for the diagnostic method). (c) Map of the relative standard deviation from the mean of JJA daytime V_{d,O_3} for forests and (d) the ratio of maximum and minimum values across the period 1980–2014.

6. Influence of Changes in Ozone Deposition on Surface Ozone

We discuss in this section the influence on simulated surface O_3 from changes in tracer dry deposition velocities. We conduct two 10-year AM4 simulations (2005–2014) at ~100 × 100-km^2 horizontal resolution, each using AM3-like full chemistry, winds nudged to National Centers for Environmental Prediction reanalysis (Lin et al., 2012; Lin et al., 2015; Lin et al., 2017), and the same anthropogenic emissions (Hoesly et al., 2018; Schnell et al., 2018), but with different dry deposition velocities, one using the default AM4 dry deposition velocities obtained from the Wesely scheme implemented in the GEOS-Chem model (Silva & Heald, 2018), the other using deposition velocities calculated from GFDL LM4.0 driven by observed atmospheric forcings (AM4_LM4dd). We focus our evaluation on the seasonal mean of the maximum daily 8-hr average (MDA8) O_3 over 2005–2014, a period when monitoring sites were densely clustered across midlatitude North America and Europe. TOAR observations are relatively sparse over East
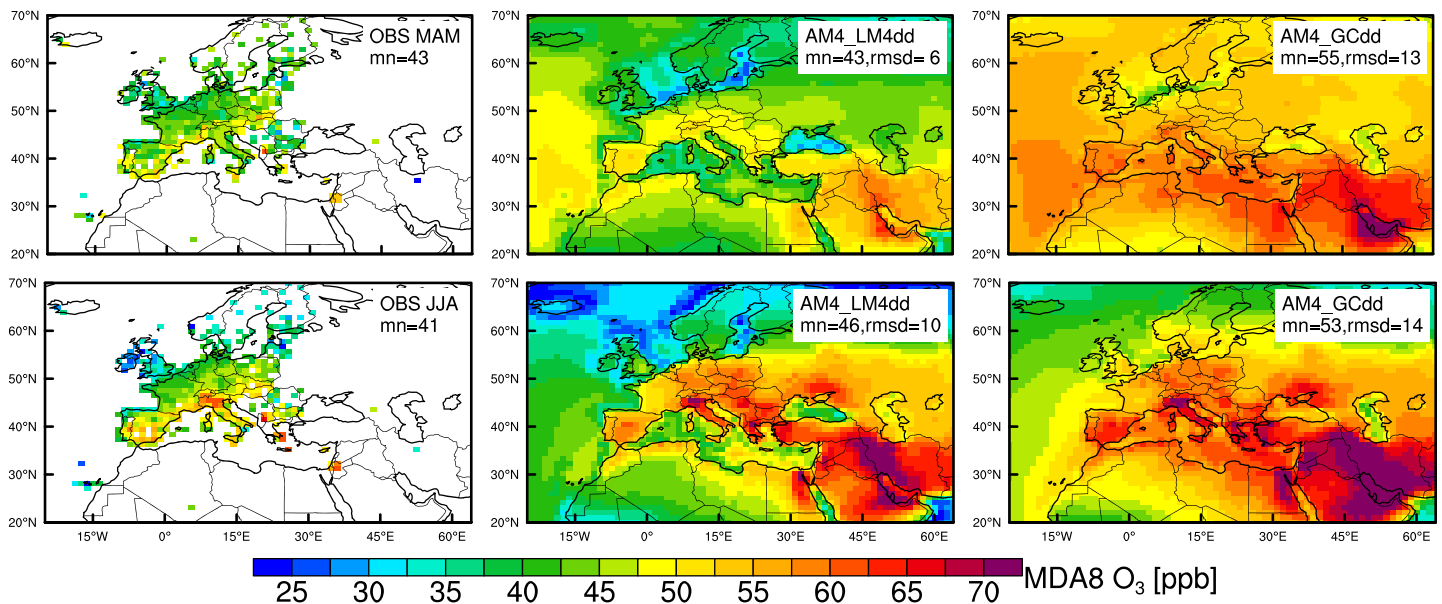
Figure 13. March-April-May (MAM) and June-July-August (JJA) mean surface MDA8 O_3 mixing ratios over Europe averaged over 2005–2014 from observations and AM4 simulations with V_{d,O_3} from GFDL-LM4.0 (AM4_LM4dd) versus from the Wesely scheme as implemented in GEOS-Chem (AM4_GCdd). Here and in other figures, mn is the mean and rmsd is the root-mean-square deviation between observations and simulations.

Asia. Thus, we additionally draw upon surface O_3 observations available during 2013–2017 from China's Ministry of Environmental Protection (CNMEP).

Spring and summertime mean surface MDA8 O_3 as observed and simulated by the two AM4 simulations, along with comparisons of V_{d,O_3}, are shown in Figures 13 and 14 for western Europe, Figures 15 and 16
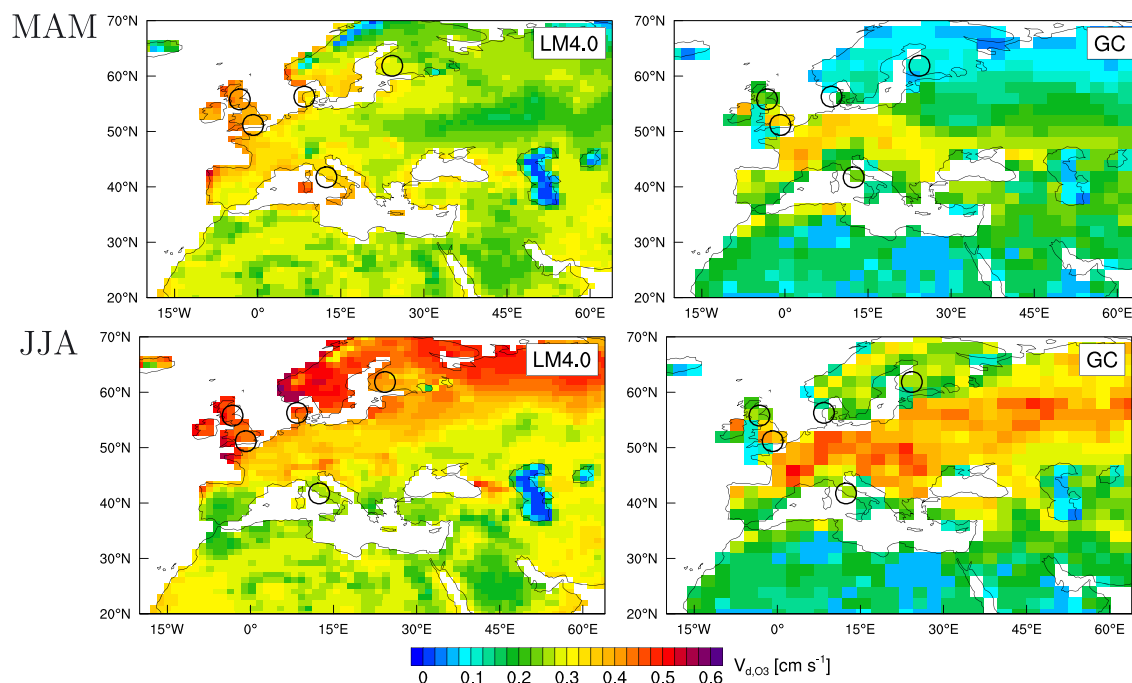

Figure 14. March-April-May (MAM) and June-July-August (JJA) 24-hr mean V_{d,O_3} over Europe from GFDL-LM4.0 versus from the Wesely scheme as implemented in GEOS-Chem (2005–2014 average). The circles denote the locations of V_{d,O_3} measurement sites to facilitate comparisons with data shown in Figures 2 and 5.
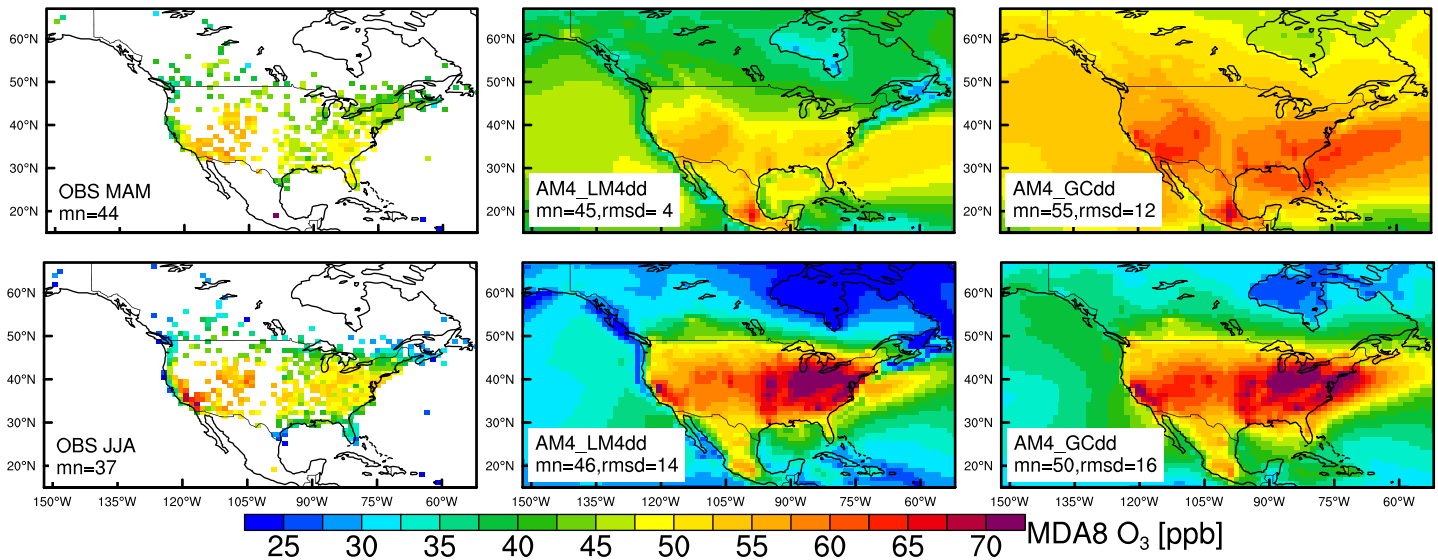
Figure 15. Same as Figure 13 but for North America.

for North America, and Figures 17 and 18 for East Asia. Using $V_{d,O3}$ from LM4.0 leads to a reduction of springtime mean MDA8 O_3 biases by ~10 ppbv and of root-mean-square deviation by ~8 ppbv throughout Northern Hemisphere in AM4 compared to using $V_{d,O3}$ from the Wesely scheme in GEOS-Chem. For summer, the improvement is most prominent at northern high latitudes (above 45°N) where coniferous trees dominate in LM4.0. Some of these improvements reflect changes in the nonstomatal deposition parameterizations in LM4.0, including a more realistic treatment of ground resistance over nonvegetated surfaces (affecting $V_{d,O3}$ over North Africa, western United States, and western China) and cuticular resistance over coniferous forests (Paulot et al., 2018). The height of the bottom atmospheric layer (centered at 35 m in LM4/AM4 and 60 m in GEOS-Chem) may influence mean $V_{d,O3}$ levels simulated in the models. Nevertheless, $V_{d,O3}$ from LM4.0 agrees well with observations, while GEOS-Chem underestimates observed JJA mean $V_{d,O3}$ at northern European coniferous forest sites by a factor of 2 (comparing Figure 14 with
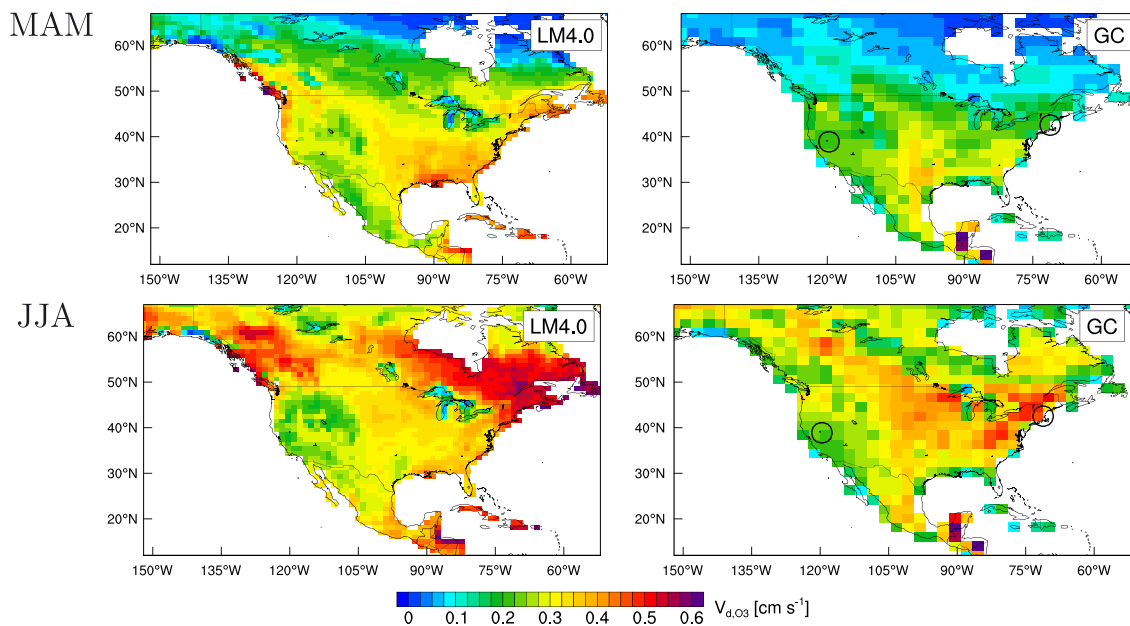

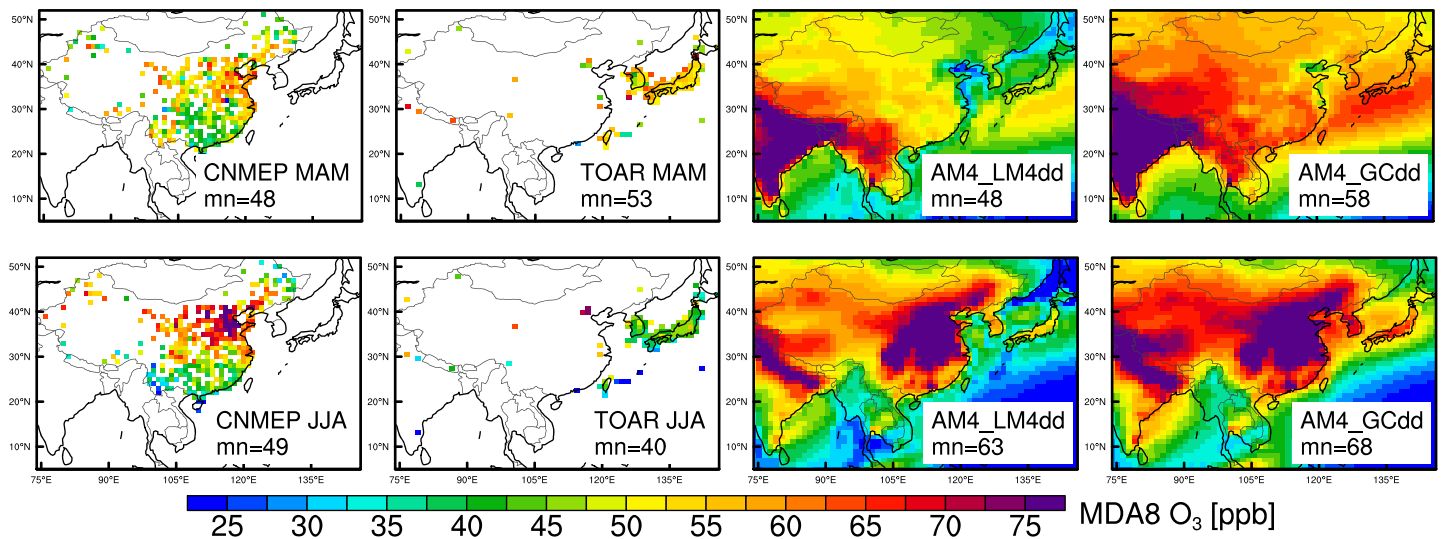**Figure 16.** Same as Figure 14 but for North America.

Figure 17. MAM and JJA mean surface MDA8 O_3 mixing ratios over East Asia from CNMEP observations (2013–2017), TOAR observations (2005–2014), and AM4 simulations (2005–2014) with $V_{d,O3}$ from GFDL-LM4 versus from the Wesely scheme as implemented in GEOS-Chem.

observations in Figure 2). Furthermore, the spatial and seasonal variability of stomatal deposition in LM4.0 is dynamic, depending not only on LAI but also on climate conditions via their effects on plant functioning. In contrast, $V_{d,O3}$ from the Wesely scheme in GEOS-Chem generally increases from spring to summer, simply scaling with the seasonal changes in LAI (Silva & Heald, 2018), not accounting for variations during the wet versus dry season that are inferred from observations (section 3.3) and from LM4.0 simulations for Mediterranean Europe, the U.S. Pacific Northwest, Mexico, and South Asia (Figures 14, 16, and 18). Silva and Heald (2018) showed that the Wesely scheme in GEOS-Chem generally reproduces the seasonal mean observed $V_{d,O3}$ averaged across sites globally but has limited skill ($R^2 = 0.04$) in simulating the site-to-site variations in observations, supporting that the Wesely scheme has a lack of sensitivity to local environmental variables.
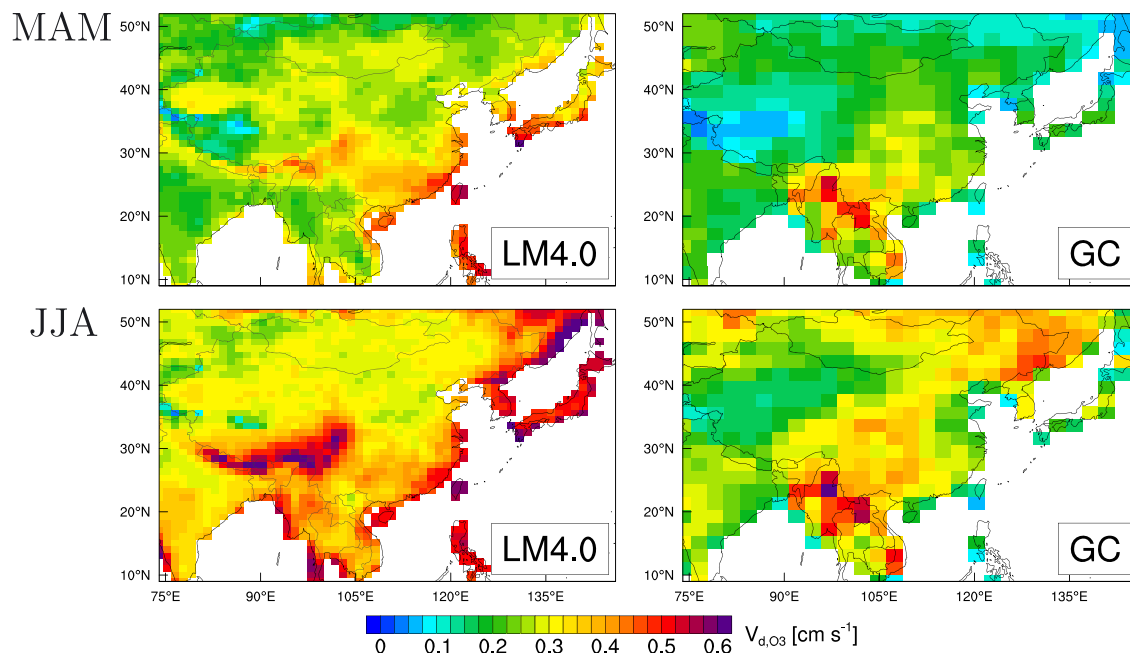

Figure 18. Same as Figure 14 but for East Asia. CNMEP = China's Ministry of Environmental Protection; JJA = June-July-August; MAM = March-April-May; TOAR = Tropospheric Ozone Assessment Report.

We note that summertime surface O_3 in the AM4_LM4dd simulations are still biased high over populated regions of the eastern United States, western Europe, and eastern China, as in many other global models (Young et al., 2018). Since LM4.0 does not have systematic biases in V_{d,O_3} over these regions during the growing season, we suggest that these surface O_3 biases may reflect some other uncertainties, such as in isoprene chemistry, chemical O_3 loss, regional O_3 precursor emissions, and difficulty in resolving O_3 vertical gradients (Fiore et al., 2014; Lin et al., 2017; Travis et al., 2016).

7. Conclusions and Recommendations

Using observations and model simulations of dynamic vegetation and atmospheric chemistry over the past half century (1960–2014), we explore the role of ecosystem-atmosphere interactions on O_3 dry deposition and air quality. Our observational analysis supports a key role for water availability in modulating O_3 deposition variability on seasonal to interannual time scales via changes in stomatal conductance, with the effects on monthly mean daytime V_{d,O_3} variability as large as a factor of 2.

We evaluate an interactive O_3 dry deposition scheme within the GFDL LM3.0 and LM4.0 dynamic vegetation land models driven by observed atmospheric forcings. An improved simulation of several important properties of vegetation in LM4.0 relative to LM3.0, including the geographical distribution of vegetation types and LAI, reduces biases in the simulation of V_{d,O_3} seasonality at some observational sites (Figures 1–3). Compared to the widely used Wesely scheme, the most novel feature of the GFDL dry deposition scheme is the photosynthesis-based parameterization of O_3 stomatal deposition as a function of phenology, soil moisture, vapor pressure deficit, and CO_2 concentration. These new features allow the models to represent successfully the observed V_{d,O_3} variability during the dry versus wet season over evergreen forests in Mediterranean Europe, South Asia, and the Amazon (Figures 4–7). On interannual time scales, large-scale drought can reduce V_{d,O_3} by ~50%, as we demonstrated with observations at a coniferous forest in Europe and at a deciduous forest in North America, consistent with the stand-alone LM3.0/LM4.0 simulations (Figures 8 and 9). Our modeling analysis, as supported by multiple observational data sets, suggests that limitation in stomatal conductance due to soil moisture deficits (as opposed to LAI changes) is the primary driver of V_{d,O_3} variability during large-scale drought events. On basis of data over one forest site, Clifton et al. (2019) notice enhanced nonstomatal O_3 deposition in dry years associated with greater soil uptake. This effect is not parameterized in our model and its significance for driving V_{d,O_3} variability during subcontinental to continental scale drought events (e.g., in summer 2003 across Europe) requires further investigation.

Climate change may reduce the reliability of water supplies that are important for both society and ecosystems. The modeling system presented in this study offers new research opportunities to study how climate change and water availability influence air quality via changes in pollutant deposition sinks to vegetation, a process that is often overlooked in current air quality projections. Changes in O_3 deposition associated with seasonal hydroclimate variability may modulate surface O_3 seasonality, such as worsening the buildup of surface O_3 pollution during the dry season. On interannual time scales, the model suggests that, over northern midlatitude forested regions, monthly mean V_{d,O_3} for the highest year is 2 to 4 times that of the lowest, with significant implications for surface O_3 variability (Figure 12). Specifically, we show that summertime V_{d,O_3} over European forests varies strongly on interannual to multidecadal time scales over the period 1960–2014, correlating with an index of drought (Figure 10). A forthcoming manuscript will explore how these changes influence the observed historical surface O_3 trends and pollution extremes. Feedbacks from ecosystem-atmosphere interactions and associated changes in O_3 deposition will impact the severity of extreme surface O_3 pollution episodes in present and future climates.

There are several limitations in the current version of our dry deposition models, such as neglect of in-canopy chemistry, inclusion of which may scavenge O_3 and reduce simulated biases with respect to observations, and neglect of possible detrimental impacts on vegetation from exposure to O_3 (e.g., Sadiq et al., 2017; Zhou et al., 2018), which may be responsible for a decrease in carbon assimilation up to 20% (Lombardozzi et al., 2012; Lombardozzi et al., 2015). Given the complexity of various, sometimes offsetting, factors influencing O_3 deposition, future work should further explore the importance of stomatal versus nonstomatal processes in driving V_{d,O_3} variability. It is also important to recognize that the land model forcing data set, particularly

precipitation, can have a substantial influence on simulated O_3 deposition. We show that the GFDL land model coupled to an atmospheric model, which has low-precipitation biases over Europe, simulates a factor of 2 weaker interannual variability in V_{d,O_3} than the simulations driven by observed atmospheric forcings (Figure 10). Generally, current climate models have difficulty in accurately simulating hydroclimate variability, particularly the spatial extent, duration, and intensity of regional drought extremes (Nasrollahi et al., 2015; Shepherd, 2014; Ukkola et al., 2018). Thus, accurate assessment of ecosystem-atmosphere interactions and future climate impacts on O_3 air quality will benefit from improved representation of hydroclimate means and extreme events in coupled atmosphere-ocean-land models.

Advancing knowledge on air quality and ecosystem-atmosphere interactions will benefit from long-term measurements of O_3 fluxes, in parallel with carbon fluxes and all supporting measurements. Our model indicates that interannual variability in summertime V_{d,O_3} to forests, driven primarily by the stomatal pathways, is largest (15–35%) in semiarid regions of western Europe, eastern North America, and northeastern China (Figure 12). Knowledge of the level of regional V_{d,O_3} variability may be used to guide deployment of key measurement sites intended to track long-term trends in the exchanges of O_3, carbon, and water between terrestrial ecosystems and the atmosphere in response to environmental stresses. New opportunities arise in implementing existing ecological monitoring networks, such as FLUXNET (http://fluxnet.fluxdata.org) and Integrated Carbon Observation System (https://www.icos-ri.eu/icosresearch-infrastructure) currently investigating CO_2 fluxes and plant ecophysiology (Fares et al., 2018). Adding O_3 sensors to key agricultural and forest sites in the established networks would represent a win-win strategy.

Data Availability Statement

Monthly mean deposition velocities from the LM4.0 simulations used in this study are archived at a public data repository at NOAA GFDL (ftp://data1.gfdl.noaa.gov/users/Meiyun.Lin/GBC2019/GFDL-LM4/).

References

Andersson, C., & Engardt, M. (2010). European ozone in a future climate: Importance of changes in dry deposition and isoprene emissions. *Journal of Geophysical Research*, *115*, D02303. https://doi.org/10.1029/2008jd011690

Begueria, S., Vicente-Serrano, S. M., Reig, F., & Latorre, B. (2014). Standardized precipitation evapotranspiration index (SPEI) revisited: Parameter fitting, evapotranspiration models, tools, datasets and drought monitoring. *International Journal of Climatology*, *34*(10), 3001–3023. https://doi.org/10.1002/joc.3887

Clifton, O. E. (2018). Constraints on ozone removal by land and implications for 21st Century ozone pollution (Doctoral dissertation). Retrieved from Columbia University Libraries (https://doi.org/10.7916/D8709J8T). New York, NY: Columbia University.

Clifton, O. E., Fiore, A. M., Munger, J. W., Malyshev, S., Horowitz, L. W., Shevliakova, E., et al. (2017). Interannual variability in ozone removal by a temperate deciduous forest. *Geophysical Research Letters*, *44*, 542–552. https://doi.org/10.1002/2016gl070923

Clifton, O. E., Fiore, A. M., Munger, J. W., & Wehr, R. (2019). Spatiotemporal controls on observed daytime ozone deposition velocity over northeastern U.S. forests during summer. *Journal of Geophysical Research: Atmospheres*, *124*, 5612–5628. https://doi.org/10.1029/2018JD029073

Coyle, M., Fowler, D., Nemitz, E., Philips, G., Storeton-West, R., Thomas, R., 2006. Field measurements of the ozone flux to vegetation. In: Ozone umbrella: Effects of ground-level ozone on (upland) vegetation in the UK. Centre of Ecology and Hydrology, UK, pp. 68–104. CEH C02158 Report No. AS 06/02.

Coyle, M., Nemitz, E., Storeton-West, R., Fowler, D., & Cape, J. N. (2009). Measurements of ozone deposition to a potato canopy. *Agricultural and Forest Meteorology*, *149*(3-4), 655–666. https://doi.org/10.1016/j.agrformet.2008.10.020

Donner, L. J., Wyman, B. L., Hemler, R. S., Horowitz, L. W., Ming, Y., Zhao, M., et al. (2011). The dynamical core, physical parameterizations, and basic simulation characteristics of the atmospheric component AM3 of the GFDL global coupled model CM3. *Journal of Climate*, *24*(13), 3484–3519. https://doi.org/10.1175/2011jcli3955.1

Dunne, J. P., John, J. G., Adcroft, A. J., Griffies, S. M., Hallberg, R. W., Shevliakova, E., et al. (2012). GFDL's ESM 2 global coupled climate-carbon Earth system models. Part I: Physical formulation and baseline simulation characteristics. *Journal of Climate*, *25*(19), 6646–6665. https://doi.org/10.1175/Jcli-D-11-00560.1

El-Madany, T. S., Niklasch, K., & Klemm, O. (2017). Stomatal and non-stomatal turbulent deposition flux of ozone to a managed peatland. *Atmosphere*, *8*(9). https://doi.org/10.3390/atmos8090175

Emberson, L. D., Kitwiroon, N., Beevers, S., Buker, P., & Cinderby, S. (2013). Scorched Earth: How will changes in the strength of the vegetation sink to ozone deposition affect human health and ecosystems? *Atmospheric Chemistry and Physics*, *13*(14), 6741–6755. https://doi.org/10.5194/acp-13-6741-2013

Fan, S. M., Wofsy, S. C., Bakwin, P. S., Jacob, D. J., & Fitzjarrald, D. R. (1990). Atmosphere-biosphere exchange of CO_2 and O_3 in the central-Amazon-forest. *Journal of Geophysical Research*, *95*(D10), 16,851–16,864. https://doi.org/10.1029/JD095iD10p16851

Fares, S., Conte, A., & Chabbi, A. (2018). Ozone flux in plant ecosystems: New opportunities for long-term monitoring networks to deliver ozone-risk assessments. *Environemental Science and Pollution Research*, *25*(9), 8240–8248. https://doi.org/10.1007/s11356-017-0352-0

Fares, S., McKay, M., Holzinger, R., & Goldstein, A. H. (2010). Ozone fluxes in a Pinus ponderosa ecosystem are dominated by non-stomatal processes: Evidence from long-term continuous measurements. *Agricultural and Forest Meteorology*, *150*(3), 420–431. https://doi.org/10.1016/j.agrformet.2010.01.007

Fares, S., Savi, F., Muller, J., Matteucci, G., & Paoletti, E. (2014). Simultaneous measurements of above and below canopy ozone fluxes help partitioning ozone deposition between its various sinks in a Mediterranean Oak Forest. *Agricultural and Forest Meteorology*, *198*, 181–191. https://doi.org/10.1016/j.agrformet.2014.08.014

Fares, S., Weber, R., Park, J. H., Gentner, D., Karlik, J., & Goldstein, A. H. (2012). Ozone deposition to an orange orchard: Partitioning between stomatal and non-stomatal sinks. *Environmental Pollution*, *169*, 258–266. https://doi.org/10.1016/j.envpol.2012.01.030

Finkelstein, P. L., Ellestad, T. G., Clarke, J. F., Meyers, T. P., Schwede, D. B., Hebert, E. O., & Neal, J. A. (2000). Ozone and sulfur dioxide dry deposition to forests: Observations and model evaluation. *Journal of Geophysical Research*, *105*(D12), 15,365–15,377. https://doi.org/10.1029/2000jd900185

Fiore, A. M., Oberman, J. T., Lin, M. Y., Zhang, L., Clifton, O. E., Jacob, D. J., et al. (2014). Estimating North American background ozone in U.S. surface air with two independent global models: Variability, uncertainties, and recommendations Atmos. *Environment*, *96*, 284–300. https://doi.org/10.1016/j.atmosenv.2014.07.045

Fowler, D., Flechard, C., Cape, J. N., Storeton-West, R. L., & Coyle, M. (2001). Measurements of ozone deposition to vegetation quantifying the flux, the stomatal and non-stomatal components. *Water, Air, and Soil Pollution*, *130*(1-4), 63–74. https://doi.org/10.1023/A:1012243317471

Fowler, D., Nemitz, E., Misztal, P., Di Marco, C., Skiba, U., Ryder, J., et al. (2011). Effects of land use on surface-atmosphere exchanges of trace gases and energy in Borneo: Comparing fluxes over oil palm plantations and a rainforest. *Philosophical Transactions of the Royal Society B*, *366*(1582), 3196–3209. https://doi.org/10.1098/rstb.2011.0055

Fowler, D., Pilegaard, K., Sutton, M. A., Ambus, P., Raivonen, M., Duyzer, J., et al. (2009). Atmospheric composition change: Ecosystems-atmosphere interactions. *Atmospheric Environment*, *43*(33), 5193–5267. https://doi.org/10.1016/j.atmosenv.2009.07.068

Ganzeveld, L., Ammann, C., & Loubet, B. (2015). Modelling atmosphere-biosphere exchange of ozone and nitrogen oxides. In R.-S. Massad & B. Loube (Eds.), *Review and integration of biosphere-atmosphere modelling of reactive trace gases and volatile aerosols* (pp. 85–105). Netherlands: Springer.

Gardner, W. R. (1960). Dynamic aspects of water availability to plants. *Soil Science*, *89*, 63–73. https://doi.org/10.1097/00010694-196002000-00001

Gerosa, G., Finco, A., Mereu, S., Marzuoli, R., & Ballarin-Denti, A. (2009). Interactions among vegetation and ozone, water and nitrogen fluxes in a coastal Mediterranean maquis ecosystem. *Biogeosciences*, *6*(8), 1783–1798. https://doi.org/10.5194/bg-6-1783-2009

Gerosa, G., Finco, A., Mereu, S., Vitale, M., Manes, F., & Denti, A. B. (2009). Comparison of seasonal variations of ozone exposure and fluxes in a Mediterranean Holm oak forest between the exceptionally dry 2003 and the following year. *Environmental Pollution*, *157*(5), 1737–1744. https://doi.org/10.1016/j.envpol.2007.11.025

Hardacre, C., Wild, O., & Emberson, L. (2015). An evaluation of ozone dry deposition in global scale chemistry climate models. *Atmospheric Chemistry and Physics*, *15*(11), 6419–6436. https://doi.org/10.5194/acp-15-6419-2015

Harris, I., Jones, P. D., Osborn, T. J., & Lister, D. H. (2014). Updated high-resolution grids of monthly climatic observations—The CRU TS3.10 Dataset. *International Journal of Climatology*, *34*(3), 623–642. https://doi.org/10.1002/joc.3711

Hoesly, R. M., Smith, S. J., Feng, L., Klimont, Z., Janssens-Maenhout, G., Pitkanen, T., et al. (2018). Historical (1750–2014) anthropogenic emissions of reactive gases and aerosols from the Community Emissions Data System (CEDS). *Geoscientific Model Development*, *11*(1), 369–408. https://doi.org/10.5194/gmd-11-369-2018

Huang, L., McDonald-Buller, E. C., McGaughey, G., Kimura, Y., & Allen, D. T. (2016). The impact of drought on ozone dry deposition over eastern Texas. *Atmospheric Environment*, *127*, 176–186. https://doi.org/10.1016/j.atmosenv.2015.12.022

Hurtt, G. C., Chini, L. P., Frolking, S., Betts, R. A., Feddema, J., Fischer, G., et al. (2011). Harmonization of land-use scenarios for the period 1500–2100: 600 years of global gridded annual land-use transitions, wood harvest, and resulting secondary lands. *Climatic Change*, *109*(1-2), 117–161. https://doi.org/10.1007/s10584-011-0153-2

Iio, A., & A. Ito (2014), A global database of field-observed leaf area index in woody plant species, 1932–2011. Data set. Available on-line [http://daac.ornl.gov] from Oak Ridge National Laboratory Distributed Active Archive Center, Oak Ridge, Tennessee, USA, edited.

Jarvis, P. G. (1976). Interpretation of variations in leaf water potential and stomatal conductance found in canopies in field. *Philosophical Transactions of the Royal Society B*, *273*(927), 593–610. https://doi.org/10.1098/rstb.1976.0035

Kavassalis, S. C., & Murphy, J. G. (2017). Understanding ozone-meteorology correlations: A role for dry deposition. *Geophysical Research Letters*, *44*, 2922–2931. https://doi.org/10.1002/2016gl071791

Kukkonen, J., Olsson, T., Schultz, D. M., Baklanov, A., Klein, T., Miranda, A. I., et al. (2012). A review of operational, regional-scale, chemical weather forecasting models in Europe. *Atmospheric Chemistry and Physics*, *12*(1), 1–87. https://doi.org/10.5194/acp-12-1-2012

Kurpius, M. R., McKay, M., & Goldstein, A. H. (2002). Annual ozone deposition to a Sierra Nevada ponderosa pine plantation. *Atmospheric Environment*, *36*(28), 4503–4515. https://doi.org/10.1016/S1352-2310(02)00423-5

Lamaud, E., Carrara, A., Brunet, Y., Lopez, A., & Druilhet, A. (2002). Ozone fluxes above and within a pine forest canopy in dry and wet conditions. *Atmospheric Environment*, *36*(1), 77–88. https://doi.org/10.1016/S1352-2310(01)00468-X

Lammertsma, E. I., de Boer, H. J., Dekker, S. C., Dilcher, D. L., Lotter, A. F., & Wagner-Cremer, F. (2011). Global CO_2 rise leads to reduced maximum stomatal conductance in Florida vegetation. *Proceedings of the National Academy of Sciences of the United States of America*, *108*(10), 4035–4040. https://doi.org/10.1073/pnas.1100371108

Leuning, R. (1995). A critical-appraisal of a combined stomatal-photosynthesis model for C-3 plants. *Plant, Cell & Environment*, *18*(4), 339–355. https://doi.org/10.1111/j.1365-3040.1995.tb00370.x

Lin, M., Fiore, A. M., Horowitz, L. W., Cooper, O. R., Naik, V., Holloway, J., et al. (2012). Transport of Asian ozone pollution into surface air over the western United States in spring. *Journal of Geophysical Research*, *117*, D00V07. https://doi.org/10.1029/2011jd016961

Lin, M., Fiore, A. M., Horowitz, L. W., Langford, A. O., Oltmans, S. J., Tarasick, D., & Rieder, H. E. (2015). Climate variability modulates western U.S. ozone air quality in spring via deep stratospheric intrusions. *Nature Communications*, *6*(7105). https://doi.org/10.1038/ncomms8105

Lin, M., Horowitz, L. W., Payton, R., Fiore, A. M., & Tonnesen, G. (2017). US surface ozone trends and extremes from 1980 to 2014: Quantifying the roles of rising Asian emissions, domestic controls, wildfires, and climate. *Atmospheric Chemistry and Physics*, *17*, 2943–2970. https://doi.org/10.5194/acp-17-2943-2017

Lombardozzi, D., Levis, S., Bonan, G., Hess, P. G., & Sparks, J. P. (2015). The influence of chronic ozone exposure on global carbon and water cycles. *Journal of Climate*, *28*(1), 292–305. https://doi.org/10.1175/Jcli-D-14-00223.1

Lombardozzi, D., Levis, S., Bonan, G., & Sparks, J. P. (2012). Predicting photosynthesis and transpiration responses to ozone: Decoupling modeled photosynthesis and stomatal conductance. *Biogeosciences*, *9*(8), 3113–3130. https://doi.org/10.5194/bg-9-3113-2012

Long, S. P., Ainsworth, E. A., Rogers, A., & Ort, D. R. (2004). Rising atmospheric carbon dioxide: Plants face the future. *Annual Review of Plant Biology*, *55*, 591–628. https://doi.org/10.1146/annurev.arplant.55.031903.141610

Malyshev, S., Shevliakova, E., Stouffer, R. J., & Pacala, S. W. (2015). Contrasting local versus regional effects of land-use-change-induced heterogeneity on historical climate: Analysis with the GFDL Earth System Model. *Journal of Climate*, *28*(13), 5448–5469. https://doi.org/10.1175/Jcli-D-14-00586.1

Manes, F., Vitale, M., Fabi, A. M., De Santis, F., & Zona, D. (2007). Estimates of potential ozone stomatal uptake in mature trees of Quercus ilex in a Mediterranean climate. *Environmental and Experimental Botany*, *59*(2), 235–241. https://doi.org/10.1016/j.envexpbot.2005.12.001

Matsuda, K., Watanabe, I., & Wingpud, V. (2005). Ozone dry deposition above a tropical forest in the dry season in northern Thailand. *Atmospheric Environment*, *39*(14), 2571–2577. https://doi.org/10.1016/j.atmosenv.2005.01.011

Matsuda, K., Watanabe, I., Wingpud, V., Theramongkol, P., & Ohizumi, T. (2006). Deposition velocity of O_3 and SO_2 in the dry and wet season above a tropical forest in northern Thailand. *Atmospheric Environment*, *40*(39), 7557–7564. https://doi.org/10.1016/j.atmosenv.2006.07.003

Mereu, S., Salvatori, E., Fusaro, L., Gerosa, G., Muys, B., & Manes, F. (2009). An integrated approach shows different use of water resources from Mediterranean maquis species in a coastal dune ecosystem. *Biogeosciences*, *6*(11), 2599–2610. https://doi.org/10.5194/bg-6-2599-2009

Meyers, T. P., Finkelstein, P., Clarke, J., Ellestad, T. G., & Sims, P. F. (1998). A multilayer model for inferring dry deposition using standard meteorological measurements. *Journal of Geophysical Research*, *103*(D17), 22,645–22,661. https://doi.org/10.1029/98jd01564

Mikkelsen, T. N., Ro-Poulsen, H., Hovmand, M. F., Jensen, N. O., Pilegaard, K., & Egelov, A. H. (2004). Five-year measurements of ozone fluxes to a Danish Norway spruce canopy. *Atmospheric Environment*, *38*(15), 2361–2371. https://doi.org/10.1016/j.atmosenv.2003.12.036

Milly, P. C. D., Malyshev, S. L., Shevliakova, E., Dunne, K. A., Findell, K. L., Gleeson, T., et al. (2014). An enhanced model of land water and energy for global hydrologic and Earth-system studies. *Journal of Hydrometeorology*, *15*(5), 1739–1761. https://doi.org/10.1175/Jhm-D-13-0162.1

Morgenstern, O., Hegglin, M. I., Rozanov, E., O'Connor, F. M., Abraham, N. L., Akiyoshi, H., et al. (2017). Review of the global models used within phase 1 of the Chemistry-Climate Model Initiative (CCMI). *Geoscientific Model Development*, *10*(2), 639–671. https://doi.org/10.5194/gmd-10-639-2017

Munger, J. W., Wofsy, S. C., Bakwin, P. S., Fan, S. M., Goulden, M. L., Daube, B. C., et al. (1996). Atmospheric deposition of reactive nitrogen oxidesand ozone in a temperate deciduous forest and a subarcticwoodland: 1. Measurements and mechanisms. *Journal of Geophysical Research Atmospheres*, *101*, 12,639–12,657. https://doi.org/10.1029/96JD00230

Nasrollahi, N., AghaKouchak, A., Cheng, L., Damberg, L., Phillips, T. J., Miao, C., et al. (2015). How well do CMIP5 climate simulations replicate historical trends and patterns of meteorological droughts? *Water Resources Research*, *51*, 2847–2864. https://doi.org/10.1002/2014wr016318

Padro, J. (1996). Summary of ozone dry deposition velocity measurements and model estimates over vineyard, cotton, grass and deciduous forest in summer. *Atmospheric Environment*, *30*(13), 2363–2369. https://doi.org/10.1016/1352-2310(95)00352-5

Park, R. J., Hong, S. K., Kwon, H. A., Kim, S., Guenther, A., Woo, J. H., & Loughner, C. P. (2014). An evaluation of ozone dry deposition simulations in East Asia. *Atmospheric Chemistry and Physics*, *14*(15), 7929–7940. https://doi.org/10.5194/acp-14-7929-2014

Paulot, F., Malyshev, S., Nguyen, T., Crounse, J. D., Shevliakova, E., & Horowitz, L. W. (2018). Representing sub-grid scale variations in nitrogen deposition associated with land use in a global Earth System Model: Implications for present and future nitrogen deposition fluxes over North America. *Atmospheric Chemistry and Physics*, *18*, 17,963–17,978. https://doi.org/10.5194/acp-18-17963-2018

Pilegaard, K., Jensen, N. O., & Hummelshoj, P. (1995). Seasonal and diurnal variation in the deposition velocity of ozone over a spruce forest in Denmark. *Water, Air, and Soil Pollution*, *85*(4), 2223–2228. https://doi.org/10.1007/Bf01186164

Rannik, U., Altimir, N., Mammarella, I., Bäck, J., Rinne, J., Ruuskanen, T. M., et al. (2012). Ozone deposition into a boreal forest over a decade of observations: Evaluating deposition partitioning and driving variables. *Atmospheric Chemistry and Physics*, *12*(24), 12,165–12,182. https://doi.org/10.5194/acp-12-12165-2012

Rummel, U., Ammann, C., Kirkman, G. A., Moura, M. A. L., Foken, T., Andreae, M. O., & Meixner, F. X. (2007). Seasonal variation of ozone deposition to a tropical rain forest in southwest Amazonia. *Atmospheric Chemistry and Physics*, *7*(20), 5415–5435. https://doi.org/10.5194/acp-7-5415-2007

Rydsaa, J. H., Stordal, F., Gerosa, G., Finco, A., & Hodnebrog, O. (2016). Evaluating stomatal ozone fluxes in WRF-Chern: Comparing ozone uptake in Mediterranean ecosystems. *Atmospheric Environment*, *143*, 237–248. https://doi.org/10.1016/j.atmosenv.2016.08.057

Sadiq, M., Tai, A. P. K., Lombardozzi, D., & Val Martin, M. (2017). Effects of ozone-vegetation coupling on surface ozone air quality via biogeochemical and meteorological feedbacks. *Atmospheric Chemistry and Physics*, *17*, 3055–3066. https://doi.org/10.5194/acp-17-3055-2017

Schnell, J., Naik, V., Horowitz, L. W., Paulot, F., Mao, J., Ginoux, P., et al. (2018). Exploring the relationship between surface PM2.5 and meteorology in Northern India. *Atmospheric Chemistry and Physics*, *18*, 10,157–10,175.

Schultz, M. G., Schröder, S., Lyapina, O., Cooper, O., Galbally, I., Petropavlovskikh, I., et al. (2017). Tropospheric ozone assessment report: Database and metrics data of global surface ozone observations. *Elementa: Science of the Anthropocene*, *5*(0). https://doi.org/10.1525/elementa.244

Seneviratne, S. I., Luthi, D., Litschi, M., & Schar, C. (2006). Land-atmosphere coupling and climate change in Europe. *Nature*, *443*(7108), 205–209. https://doi.org/10.1038/nature05095

Sheffield, J., Goteti, G., & Wood, E. F. (2006). Development of a 50-year high-resolution global dataset of meteorological forcings for land surface modeling. *Journal of Climate*, *19*(13), 3088–3111. https://doi.org/10.1175/Jcli3790.1

Shepherd, T. G. (2014). Atmospheric circulation as a source of uncertainty in climate change projections. *Nature Geoscience*, *7*(10), 703–708. https://doi.org/10.1038/Ngeo2253

Shevliakova, E., Pacala, S. W., Malyshev, S., Hurtt, G. C., Milly, P. C. D., Caspersen, J. P., et al. (2009). Carbon cycling under 300 years of land use change: Importance of the secondary vegetation sink. *Global Biogeochemical Cycles*, *23*, GB2022. https://doi.org/10.1029/2007gb003176

Silva, S. J., & Heald, C. L. (2018). Investigating dry deposition of ozone to vegetation. *Journal of Geophysical Research: Atmospheres*, *123*, 559–573. https://doi.org/10.1002/2017jd027278

Simpson, D., Benedictow, A., Berge, H., Bergström, R., Emberson, L. D., Fagerli, H., et al. (2012). The EMEP MSC-W chemical transport model—Technical description. *Atmospheric Chemistry and Physics*, *12*(16), 7825–7865. https://doi.org/10.5194/acp-12-7825-2012

Sitch, S., Cox, P. M., Collins, W. J., & Huntingford, C. (2007). Indirect radiative forcing of climate change through ozone effects on the land-carbon sink. *Nature*, *448*(7155), 791–U794. https://doi.org/10.1038/nature06059

Stella, P., Personne, E., Loubet, B., Lamaud, E., Ceschia, E., Béziat, P., et al. (2011). Predicting and partitioning ozone fluxes to maize crops from sowing to harvest: The Surfatm-O-3 model. *Biogeosciences*, *8*(10), 2869–2886. https://doi.org/10.5194/bg-8-2869-2011

Stevenson, D. S., Dentener, F. J., Schultz, M. G., Ellingsen, K., van Noije, T. P. C., Wild, O., et al. (2006). Multimodel ensemble simulations of present-day and near-future tropospheric ozone. *Journal of Geophysical Research*, *111*, D08301. https://doi.org/10.1029/2005jd006338

Travis, K. R., Jacob, D. J., Fisher, J. A., Kim, P. S., Marais, E. A., Zhu, L., et al. (2016). Why do models overestimate surface ozone in the Southeast United States? *Atmospheric Chemistry and Physics*, *16*(21), 13,561–13,577. https://doi.org/10.5194/acp-16-13561-2016

Turnipseed, A. A., Burns, S. P., Moore, D. J. P., Hu, J., Guenther, A. B., & Monson, R. K. (2009). Controls over ozone deposition to a high elevation subalpine forest. *Agricultural and Forest Meteorology*, *149*(9), 1447–1459. https://doi.org/10.1016/j.agrformet.2009.04.001

Ukkola, A. M., Pitman, A. J., De Kauwe, M. G., Abramowitz, G., Herger, N., Evans, J. P., & Decker, M. (2018). Evaluating CMIP5 model agreement for multiple drought metrics. *Journal of Hydrometeorology*, *19*(6), 969–988. https://doi.org/10.1175/Jhm-D-17-0099.1

Val Martin, M., Heald, C. L., & Arnold, S. R. (2014). Coupling dry deposition to vegetation phenology in the Community Earth SystemModel: Implications for the simulation of surface O_3. *Geophysical Research Letters*, *41*, 2988–2996. https://doi.org/10.1002/2014GL059651

Weng, E. S., Malyshev, S., Lichstein, J. W., Farrior, C. E., Dybzinski, R., Zhang, T., et al. (2015). Scaling from individual trees to forests in an Earth system modeling framework using a mathematically tractable model of height-structured competition. *Biogeosciences*, *12*(9), 2655–2694. https://doi.org/10.5194/bg-12-2655-2015

Wesely, M. L. (1989). Parameterization of surface resistances to gaseous dry deposition in regional-scale numerical models. *Atmospheric Environment*, *23*, 1293–1304. https://doi.org/10.1016/0004-6981(89)90153-4

Wesely, M. L., & Hicks, B. B. (2000). A review of the current status of knowledge on dry deposition. *Atmospheric Environment*, *34*(12-14), 2261–2282. https://doi.org/10.1016/S1352-2310(99)00467-7

Wild, O. (2007). Modelling the global tropospheric ozone budget: Exploring the variability in current models. *Atmospheric Chemistry and Physics*, *7*(10), 2643–2660. https://doi.org/10.5194/acp-7-2643-2007

Wu, Z., Schwede, D., Vet, R., Walker, J. T., Shaw, M., Staebler, R., & Zhang, L. (2018). Evaluation and intercomparison of five major dry deposition algorithms in North America. *Journal of Advances in Modeling Earth Systems*, *10*, 1571–1586. https://doi.org/10.1029/2017MS001231

Wu, Z. Y., Staebler, R., Vet, R., & Zhang, L. M. (2016). Dry deposition of O_3 and SO_2 estimated from gradient measurements above a temperate mixed forest. *Environmental Pollution*, *210*, 202–210. https://doi.org/10.1016/j.envpol.2015.11.052

Wu, Z. Y., Zhang, L., Wang, X. M., & Munger, J. W. (2015). A modified micrometeorological gradient method for estimating O_3 dry depositions over a forest canopy. *Atmospheric Chemistry and Physics*, *15*(13), 7487–7496. https://doi.org/10.5194/acp-15-7487-2015

Young, P. J., Archibald, A. T., Bowman, K. W., Lamarque, J. F., Naik, V., Stevenson, D. S., et al. (2013). Pre-industrial to end 21st century projections of tropospheric ozone from the Atmospheric Chemistry and Climate Model Intercomparison Project (ACCMIP). *Atmospheric Chemistry and Physics*, *13*(4), 2063–2090. https://doi.org/10.5194/acp-13-2063-2013

Young, P. J., Naik, V., Fiore, A. M., Gaudel, A., Guo, J., Lin, M. Y., et al. (2018). Tropospheric ozone assessment report: Assessment of global-scale model performance for global and regional ozone distributions, variability, and trends. *Elementa: Science of the Anthropocene*, *6*(1). https://doi.org/10.1525/elementa.265

Zapletal, M., Cudlín, P., Chroust, P., Urban, O., Pokorný, R., Edwards-Jonášová, M., et al. (2011). Ozone flux over a Norway spruce forest and correlation with net ecosystem production. *Environmental Pollution*, *159*(5), 1024–1034. https://doi.org/10.1016/j.envpol.2010.11.037

Zhang, L. M., Brook, J. R., & Vet, R. (2002). On ozone dry deposition—With emphasis on non-stomatal uptake and wet canopies. *Atmospheric Environment*, *36*(30), 4787–4799. https://doi.org/10.1016/S1352-2310(02)00567-8

Zhang, L. M., Brook, J. R., & Vet, R. (2003). A revised parameterization for gaseous dry deposition in air-quality models. *Atmospheric Chemistry and Physics*, *3*, 2067–2082. https://doi.org/10.5194/acp-3-2067-2003

Zhang, L. M., Vet, R., Brook, J. R., & Legge, A. H. (2006). Factors affecting stomatal uptake of ozone by different canopies and a comparison between dose and exposure. *Science of the Total Environment*, *370*(1), 117–132. https://doi.org/10.1016/j.scitotenv.2006.06.004

Zhao, M., Golaz, J. C., Held, I. M., Guo, H., Balaji, V., Benson, R., et al. (2018a). The GFDL Global Atmosphere and Land Model AM4.0/LM4.0:1. Simulation characteristics with prescribed SSTs. *Journal of Advances in Modeling Earth Systems*, *10*, 691–734. https://doi.org/10.1002/2017ms001208

Zhao, M., Golaz, J. C., Held, I. M., Guo, H., Balaji, V., Benson, R., et al. (2018b). The GFDL Global Atmosphere and Land Model AM4.0/LM4.0:2. Model description, sensitivity studies, and tuning strategies. *Journal of Advances in Modeling Earth Systems*, *10*(3), 735–769. https://doi.org/10.1002/2017ms001209

Zhou, S. S., Tai, A. P. K., Sun, S., Sadiq, M., Heald, C. L., & Geddes, J. A. (2018). Coupling between surface ozone and leaf area index in a chemical transport model: Strength of feedback and implications for ozone air quality and vegetation health. *Atmospheric Chemistry and Physics*, *18*, 14,133–14,148. https://doi.org/10.5194/acp-18-14133-2018